

**Angular Distribution Models for Top-of-Atmosphere Radiative Flux
Estimation from the Clouds and the Earth's Radiant Energy System
Instrument on the *Terra* Satellite. Part II: Validation**

Norman G. Loeb¹

Center for Atmospheric Sciences, Hampton University, Hampton, Virginia

Seiji Kato

Center for Atmospheric Sciences, Hampton University, Hampton, Virginia

Konstantin Loukachine

Science Applications International Corporation, Hampton, Virginia

Natividad Manalo-Smith, David R. Doelling

Analytical Services and Materials, Hampton, Virginia

Journal of Atmospheric and Oceanic Technology

Submitted December, 2005

¹ *Corresponding Author Address:* Dr. Norman G. Loeb, Mail Stop 420, NASA Langley Research Center, Hampton, VA 23681-2199, U.S.A.



Abstract

Errors in top-of-atmosphere (TOA) radiative fluxes from the Clouds and the Earth's Radiant Energy System (CERES) instrument due to uncertainties in radiance-to-flux conversion from CERES *Terra* Angular Distribution Models (ADMs) are evaluated through a series of consistency tests. These tests show that the overall bias in regional monthly mean shortwave (SW) TOA flux is less than 0.2 W m^{-2} and the regional RMS error ranges from 0.75 and 1.6 W m^{-2} . In contrast, SW TOA fluxes inferred using theoretical ADMs that assume clouds are plane-parallel are overestimated by 3 to 4 W m^{-2} , and exhibit a strong latitudinal dependence. In the longwave (LW), the bias error ranges from 0.2 to 0.4 W m^{-2} and regional RMS errors remain smaller than 0.7 W m^{-2} . Global mean albedos derived from ADMs developed during the Earth Radiation Budget Experiment (ERBE) and applied to CERES measurements show a systematic increase with viewing zenith angle of 4% to 8% , while albedos from the CERES *Terra* ADMs show a smaller increase of 1% - 2% . LW fluxes from the ERBE ADMs show a systematic decrease with viewing zenith angle of 2% - 2.4% , whereas fluxes from the CERES *Terra* ADMs remain within 0.7% - 0.8% at all angles. Based on several months of multiangle CERES alongtrack data, the SW TOA flux consistency between nadir and oblique viewing zenith angles is generally 5% over land and ocean and 9% in polar regions, and LW TOA flux consistency is approximate 3% over all surfaces. Monthly mean TOA fluxes based on ERBE ADMs are larger than monthly mean TOA fluxes based on CERES *Terra* ADMs by 1.8 W m^{-2} and 1.3 W m^{-2} in the SW and LW, respectively.



1. Introduction

The central objective of the Clouds and the Earth's Radiant Energy System (CERES) mission is to provide accurate global cloud, aerosol and radiation data products to facilitate research addressing the role clouds and aerosols play in modulating the radiative energy flow within the Earth-atmosphere system (Wielicki et al., 1996). A critical step in providing these data products is the conversion of measured CERES radiances to radiative fluxes. As described in detail in Part I (Loeb et al., 2005), radiative fluxes from CERES are estimated using empirical Angular Distribution Models (ADMs) that characterizes the anisotropy or angular variation of the radiation field. Since anisotropy is scene dependent, CERES uses coincident imager measurements from the Moderate Resolution Imaging Spectroradiometer (MODIS) instrument (Barnes et al., 1998) to characterize the scene within each CERES footprint. Loeb et al. (2005) and Kato and Loeb (2005) used 46 months of merged CERES and MODIS *Terra* measurements to develop a new set of global ADMs for estimating global TOA fluxes from CERES *Terra* measurements.

In this study, uncertainties in regional mean and instantaneous TOA fluxes from CERES *Terra* ADMs are estimated. We use a series of consistency tests similar to those used previously in Loeb et al. (2003b) for testing TOA fluxes from CERES measurements aboard the Tropical Rainfall Measuring Mission (*TRMM*) satellite. For comparison, TOA fluxes based on CERES *Terra* ADMs are also compared with TOA fluxes from ADMs developed on *TRMM* and *Aqua*, and with fluxes from Earth Radiation Budget Experiment (ERBE) ADMs (Smith et al., 1986; Suttles et al., 1992).



2. Observations

CERES measures radiances in a shortwave reflective channel (0.3-5 μm), a thermal (8-12 μm) “window” channel, and a total channel covering wavelengths between 0.3 and 200 μm . On *Terra*, CERES has a spatial resolution of approximately 20 km (equivalent diameter) at nadir and operates in four scan modes: cross-track, along-track, rotating azimuth plane (RAP), and programmable azimuth plane (PAP). The cross-track scan is perpendicular to the ground track and optimizes spatial sampling but has limited angular sampling; the along-track scan provides measurements near the satellite orbital plane at several near-simultaneous viewing zenith angles over the same region; and the RAP scan provides multiangle measurements at a number of viewing zenith and relative azimuth angles by scanning in elevation as it rotates in azimuth; in PAP mode, the CERES angular sampling is commanded from the ground by uploading instructions to the instrument to acquire multiangle measurements for specific scientific experiments (e.g., field campaigns, intercalibration with other instruments, etc.).

The first CERES instrument flew on the *TRMM* satellite in a 350-km circular, precessing orbit with a 35° inclination angle between January-August 1998, and March 2000, (Loeb et al., 2003a). Unfortunately, the CERES *TRMM* instrument suffered a voltage converter anomaly and acquired only 9 months of scientific data. Four CERES instruments are currently in orbit on the *Terra* and *Aqua* spacecrafts. *Terra*, launched on December 18th, 1999, carries two identical CERES instruments: Flight Models 1 (FM-1) and 2 (FM-2). *Terra* is in a descending sun-synchronous orbit with an equator crossing time of 10:30 a.m. local time. The *Aqua* spacecraft was launched on May 4th, 2002, and carries Flight Models 3 (FM-3) and 4 (FM-4). *Aqua* is in an ascending sun-synchronous orbit with an equator crossing time of 1:30 p.m. local time.

In this study, observations from the CERES *Terra* Edition2B_Rev1 Single Scanner

Footprint TOA/Surface Fluxes and Clouds (SSF) product (Geier et al., 2001) between March 2000 and December 2003 are considered. The SSF merges CERES parameters including time, position, viewing geometry, radiances and radiative fluxes with coincident information from the Moderate Resolution Imaging Spectroradiometer (MODIS), which is used to characterize the clear and cloudy portions of a CERES footprint. MODIS-SSF parameters include radiances in 5 spectral bands for clear, cloudy and total areas, cloud property retrievals (Minnis et al., 1998; Minnis et al., 2003), and aerosol property retrievals from the MOD04 product (Remer et al., 2005), and a second aerosol retrieval algorithm applied to MODIS (Ignatov and Stowe, 2002). Also included in the SSF product are meteorological parameters (e.g., surface wind speed, skin temperature, precipitable water, etc.) from the Global Modeling and Assimilation Office (GMAO)'s Goddard Earth Observing System DAS (GEOS-DAS V4.0.3) product (Suarez, 2005). In the CERES *Terra* SSF product, only CERES footprints that overlap with the MODIS imager swath are retained. Since the maximum viewing zenith angle of MODIS is 63° , few crosstrack CERES footprints with viewing zenith angles $> 63^\circ$ appear in the SSF product. Footprints at viewing zenith angles beyond this limit do however appear when CERES operates in a RAP or alongtrack scan mode.

For comparison, data from the CERES *Aqua* Edition2A_Rev1 SSF product between January-December 2003 are also considered. The ADMs used to estimate TOA fluxes on the CERES *Aqua* SSF are based on the same methodology as the *Terra* ADMs (Loeb et al., 2005; Kato and Loeb, 2005), but were developed from *Aqua* SSF measurements between August 2002 and June 2004. Differences between *Terra* and *Aqua* ADMs arise primarily from changes to the CERES cloud mask in polar regions (Minnis, personal communication).

TOA fluxes from the CERES *Terra* ADMs are also compared with TOA fluxes in the CERES ERBE-like products, which are based on ADMs derived from *Nimbus-7* observations (Suttles et al., 1988, Suttles et al., 1989). For these comparisons, we use both the instantaneous (ES-8) and monthly mean (ES-4) ERBE-like data products. The ES-4 monthly mean TOA fluxes are compared with fluxes from the TOA/Surface Averages (SRBAVG) data product, which is based on the CERES *Terra* ADMs.

3. Regional Mean TOA Flux Error

3.1 Shortwave

The standard approach for determining regional mean TOA flux errors due to ADM uncertainties is the so-called “direct integration” method (Suttles et al., 1992; Loeb et al., 2003b), whereby regionally averaged ADM-derived TOA fluxes are compared with regional mean fluxes obtained by direct integration of observed mean radiances (DI fluxes). To determine the DI fluxes, the measured radiances in a region are first stratified by viewing geometry, summed for some fixed time interval (e.g., a season), and averaged. In order to acquire enough samples in a region, the instrument must scan the full range of viewing zenith (θ) and relative azimuth angle (ϕ). This requires compositing measurements with an instrument in RAP mode over relatively large regions (e.g., $10^\circ \times 10^\circ$ latitude-longitude). The DI approach also requires uniform angular sampling in each region. That is, all portions of a $10^\circ \times 10^\circ$ latitude-longitude region should contribute equally to the mean radiances in every angular bin. Unfortunately, this condition is rarely satisfied for CERES *Terra* because *Terra*’s sun-synchronous orbit introduces a strong correlation between latitude, solar zenith angle (θ_0) and relative azimuth angle. The DI method is better suited for instruments on

spacecrafts in a precessing orbit (e.g., *TRMM*) since each region is observed from a full range of solar and viewing geometries during each precession cycle.

An alternate approach for estimating regional mean TOA flux errors due to ADM uncertainties is to use a modified version of the direct integration approach. For each CERES observed radiance, one can generate a CERES ADM-predicted radiance using the MODIS scene information and the CERES viewing geometry (Loeb et al., 2005). The observed and ADM-predicted radiances can be used to construct two separate sets of regional all-sky ADMs in all $10^\circ \times 10^\circ$ latitude-longitude regions of the Earth. A regional all-sky ADMs is constructed by sorting the radiances in a region by viewing geometry (θ_o , θ , ϕ) and evaluating the ratio of the mean radiance in an angular bin to the DI flux, obtained by integrating radiances in all angular bins (Loeb et al., 2005). Because a CERES ADM-predicted radiance is provided for every CERES observed radiance, the same sampling is used to construct both sets of regional all-sky ADMs. To ensure adequate sampling over angle, at least 3 months of RAP data are used. Next, the observed and ADM-predicted regional ADMs are applied to the same month of crosstrack data. We assume that the TOA flux difference from the two sets of ADMs is representative of the actual TOA flux error due to uncertainties in the CERES ADMs.

Figs. 1a-d show the regional mean TOA flux errors from all-sky ADMs in each season (December-February; March-May; June-August; September-November) between December 2002 and November 2003. This time period lies well outside the March 2000-February 2002 interval used by Loeb et al. (2005) to develop the *Terra* ADMs. Regional mean all-sky TOA fluxes are obtained by applying the predicted and observed all-sky $10^\circ \times 10^\circ$ regional ADMs to CERES crosstrack measurements for the middle month of each

season (i.e., January, April, July and October). Here, TOA flux errors are evaluated in each $1^\circ \times 1^\circ$ region within the larger $10^\circ \times 10^\circ$ region in order to consider the same angular sampling within a region that is used to produce the CERES monthly mean data products (Wielicki et al., 1996). The daily mean instantaneous TOA flux difference in each $1^\circ \times 1^\circ$ region is converted to an equivalent 24-hour flux difference by applying a scaling factor determined from the ratio of the total daily insolation to the mean insolation at the *Terra* overpass time(s) (the latter is determined from the daily mean cosine of solar zenith angle from the *Terra* data).

In the tropics and midlatitudes, regional mean TOA flux errors are generally $< 1.5 \text{ W m}^{-2}$. In some regions, such as over Australia in January and October, and over Saudi Arabia in July and October, positive TOA flux errors reaching 3 W m^{-2} are observed. Over ocean, TOA flux errors generally show little regional dependence, except in regions affected by desert dust, such as off the coasts of the Saharan and Saudi Arabian deserts in July. In these regions, Loeb and Manalo-Smith (2005) showed significant discrepancies between the CERES and MODIS MOD04 aerosol product (Remer et al., 2005) cloud masks. Therefore, larger TOA flux errors in these regions may be related to uncertainties in the CERES cloud/dust identification algorithm. At high latitudes, regional mean TOA flux errors are generally negative over sea-ice along the coast of Antarctica in January, and slightly positive over permanent snow regions. In the Arctic, large positive errors occur in April north of 60°N , but change to negative in July when solar insolation is a maximum. The negative TOA flux errors are especially large in regions of broken sea-ice and cloud cover over the Canadian Northwest Territories.

Zonal average regional mean TOA flux errors for each season are provided in Fig. 2a-d. TOA flux errors derived from CERES *Terra* SSFs are compared with those derived from CERES *Aqua* SSFs for the same months. The *Aqua* results utilize recently developed ADMs constructed specifically for *Aqua* from two years of *Aqua* SSFs. The *Terra* and *Aqua* regional mean TOA flux errors are generally $< 2 \text{ W m}^{-2}$ everywhere except between 70°N - 80°N in July. Table 1 summarizes the average regional shortwave (SW) TOA flux errors for *Terra* and *Aqua* in each season. In all cases, the bias is less than 0.2 W m^{-2} and the regional RMS error is between 0.75 and 1.6 W m^{-2} . These regional errors are generally consistent with the CERES accuracy goals of 0.5 to 1 W m^{-2} (Wielicki et al., 1995).

Between 70°N - 80°N in July, the *Terra* ADMs underestimate the regional mean TOA flux by approximately 10 W m^{-2} , while errors from *Aqua* ADMs remain less than 2 W m^{-2} . The cause for the difference between the *Terra* and *Aqua* results is due to scene identification differences. To illustrate, Fig. 3a shows regional SW TOA flux errors when *Terra* and *Aqua* ADMs are both applied using scene identification from MODIS *Terra*, and Fig. 3b shows the errors when MODIS *Aqua* scene identification is used. In Fig. 3a, large regional errors occur regardless of whether *Terra* or *Aqua* ADMs are used. In contrast, when scene identification from MODIS *Aqua* is used, regional TOA flux errors are reduced by a factor of 2 with the *Terra* ADMs, and a factor of 4 with the *Aqua* ADMs. Since the same methodology is used to create *Terra* and *Aqua* ADMs from CERES SSF data, the main difference between the *Terra* and *Aqua* results is due to changes in cloud algorithm. Specifically, the *Aqua* daytime polar cloud mask includes several improvements compared to *Terra* (Trepte, personal communication, 2005). These changes include the following: i) refined twilight *Aqua* cloud and snow detection; ii) improved cloud and snow detection in



transition areas between polar and non-polar regions; 3) refined polar cloud mask thresholds and the addition of a new threshold test (6.7 μm minus 11 μm brightness temperature difference) that improves the distinction between clouds and underlying snow ice surfaces. With these changes, the fraction of footprints with sufficient cloud retrievals for determination of ADM scene identification increased significantly: for July same months, the *Terra* cloud algorithm provided sufficient cloud retrievals 87% of the time for latitudes greater than 60°, compared to 94% for *Aqua*. These improvements to the CERES cloud algorithm will be included in the next edition of CERES SSF product (Edition 3).

3.1.1 Comparison with Plane-Parallel Model SW ADMs

The use of empirical ADMs is but one approach for converting measured radiances to TOA fluxes. Because the CERES SSF product provides detailed cloud properties for every CERES footprint, TOA fluxes can also be estimated using theoretical ADMs. One approach is to assume that clouds are one dimensional and use a plane-parallel radiative transfer model to characterize the anisotropy of clouds. To test this approach, we use a plane-parallel radiative transfer model to construct regional ADMs using the same approach as was used in Section 3.1. Using the CERES cloud properties as input, a plane-parallel model (1D, hereafter) radiance for a given CERES footprint is estimated as follows:

$$I_{1D}(\theta_o, \theta, \phi) = (1-f) I_{CER}^{clr}(\theta_o, \theta, \phi) + f I_{1D}^{ovc}(\theta_o, \theta, \phi; \tau, P) \quad (1)$$

where f is the MODIS-based cloud fraction within a CERES footprint, τ is the visible cloud optical depth, and P is the cloud phase (liquid water or ice). In order to minimize the influence of uncertainties in surface albedo, the comparison is restricted to ice-free ocean areas, and the radiance in the cloud-free portion of the CERES footprint is determined using clear-sky ocean CERES ADMs (Loeb et al., 2005) (I_{CER}^{clr}). In order to minimize uncertainties associated with

cloud scattering phase function, only footprints comprised of liquid water clouds are included. The radiative transfer calculations are from the *rstar5b* radiative transfer code that is based on Nakajima and Tanaka (1986, 1988). Broadband radiance calculations from the model are determined at 20 cloud optical depths between 0.1 and 200, 18 solar zenith angles, 18 viewing zenith angles and 18 relative azimuth angles. The radiative transfer calculations use the TMS (Truncated Multiple and Single) method (Nakajima and Tanaka, 1988) with 10 Gaussian quadrature points in the hemisphere for integrating the radiative transfer equation over angle. The ocean surface in the calculations accounts for the bidirectional reflectance. The liquid water cloud is at an altitude of 2 km, and its phase function is determined from Mie Theory for a droplet size distribution with an effective radius of 10 μm . A U.S. Standard Atmosphere is assumed in all calculations. To assess the uncertainty of assuming a fixed cloud-top height in the calculation, we compared anisotropic factors determined using 1-km and 3-km cloud-top heights for a solar zenith angle of 45° and a cloud optical depth of 12.5. For typical cloud conditions and CERES viewing geometries, the sensitivity to cloud-top height in the anisotropic factors was negligible ($\sim 0.3\%$).

TOA flux errors obtained using regional ADMs constructed from 1D radiances (Eq. 1) are shown in Figs. 4a-b for July and January, respectively. These are compared with TOA flux errors for regional ADMs determined with CERES ADM-predicted radiances (Figs. 4c-d). During both seasons, 1D TOA regional mean flux errors exhibit a strong latitudinal dependence—in the mid-latitude winter and high-latitude summer regions, 1D errors reach 10 W m^{-2} (24-hour average), and decrease to -5 W m^{-2} in the subtropical summer regions. A similar dependence is obtained when 1D model calculations from the CERES Clouds and Radiative Swath (CRS) product (Charlock et al., 1997) are compared with CERES TOA fluxes (not

shown). Regional mean TOA flux errors derived using CERES ADM-predicted radiances (Figs. 4c-d) are markedly better than the 1D results in Figs. 4a-b. On a global average, the mean TOA flux errors using the 1D regional ADMs are 3.3 W m^{-2} in July and 3.6 W m^{-2} in January, compared to -0.3 W m^{-2} in July and 0.3 W m^{-2} in January using the CERES ADM-predicted radiances. Because *Terra* is in a sun-synchronous orbit, the latitude-dependent biases in Figs. 4a-b are actually symptomatic of a solar zenith angle dependent bias in the 1D model fluxes. Loeb and Davies (1996) and Loeb and Coakley (1998) found similar dependencies in 1D-derived cloud optical depths retrievals. Consistent with the results in Fig. 4, those studies found that 1D-derived cloud optical depths systematically increase with solar zenith angle.

3.2 Longwave and Window

In the longwave (LW) and window (WN) regions, TOA flux is a weak function of solar zenith angle and therefore correlations between latitude, solar zenith angle and relative azimuth angle resulting from *Terra*'s sun-synchronous orbit have a negligible effect. Therefore, to determine regional mean TOA flux errors due to ADM uncertainties, we use the standard DI method (Suttles et al., 1992; Loeb et al., 2003b), whereby regionally averaged ADM-derived TOA fluxes are directly compared with regional mean fluxes obtained by direct integration of observed mean radiances (DI fluxes). Regional mean TOA flux errors are determined separately for daytime ($\theta_0 \leq 90$) and nighttime ($\theta_0 > 90$) conditions. 24-hour average TOA flux errors are obtained by averaging the daytime and nighttime results, accounting for the fraction of daylight at each latitude for each month. Regional distributions of LW TOA flux errors are shown in Figs. 5a-d for each season and summarized in Table 2. LW flux errors are generally larger over land than over ocean. For example, positive biases of up to 3 W m^{-2} are observed between 40°N - 60°N in April over Western North America, Europe and Central Asia, but not over the adjacent ocean

area. Over ocean, the flux errors are largest at higher latitudes, such as in the North Atlantic in January, and along the coast of Antarctica in January and July. Interestingly, LW TOA flux errors between 70°N-80°N in July remain $< 1 \text{ W m}^{-2}$, contrary to the large errors in that region found in SW fluxes (Fig.1c). Overall, the bias in LW TOA flux ranges from 0.2 to 0.4 W m^{-2} , and regional RMS errors remain less than 0.7 W m^{-2} for both *Terra* and *Aqua* (Table 2).

Zonal average LW flux errors for *Terra* are comparable to those for *Aqua* (Fig. 6a-d) everywhere except between 70°S and 90°S. In that latitude range, LW TOA flux errors from *Aqua* ADMs show negative biases of up to 3 W m^{-2} . The larger *Aqua* LW TOA flux bias is associated with changes in the nighttime polar cloud mask. Over the Antarctic Plateau region, modifications to the *Aqua* snow/ice thresholds for the 11 μm brightness temperature and 6.7 μm – 11 μm brightness temperature difference tests significantly reduced the cloud cover compared to *Terra* (Trepte, personal communication, 2005). Because the cloud amount changes are more pronounced at nadir than oblique viewing zenith angles, the *Aqua* LW ADMs are more anisotropic compared to the *Terra* LW ADMs. Figs. 7a-b illustrate how the cloud mask changes between *Aqua* and *Terra* influence TOA flux errors for three regions over Antarctica. For *Aqua* (Fig. 7a), overestimation of anisotropic factors at $\theta < 50^\circ$ leads to an underestimation of TOA fluxes, while the opposite occurs for $\theta > 50^\circ$. In contrast, LW TOA flux errors for *Terra* ADMs (Fig. 7b) are small and remain independent of θ . Based on these results, therefore, the CERES team has decided to use *Terra* nighttime LW permanent snow ADMs in *Aqua* Edition2A processing.

Regional mean TOA flux errors were also determined for the WN fluxes using the same approach as that used to determine LW TOA flux errors. As shown in Table 3, the overall bias in WN TOA flux is $< 0.2 \text{ W m}^{-2}$ and the regional RMS error is $< 0.35 \text{ W m}^{-2}$.

4. Instantaneous TOA Flux Uncertainties

Because the true instantaneous TOA flux for a CERES footprint is unavailable, there is no direct way of determining the actual instantaneous TOA flux error. However, an indication of TOA flux error can be obtained through a series of consistency tests that compare ADM-derived TOA fluxes of the same scene from different viewing geometries. In the following, results of several TOA flux consistency tests are presented under various conditions using several approaches.

4.1 Programmable Azimuth Plane Scans Over ARM-SGP

For the entire month of May 2003, the CERES FM2 instrument was placed in a PAP scan mode that was optimized to acquire multiangle measurements over the Department of Energy Atmospheric Radiation Measurement (ARM) Southern Great Plains (SGP) Central Facility. On these days, the CERES azimuth plane was rotated such that the ARM-SGP site remained in the CERES scan plane as *Terra* moved past the site. Figs. 8a-d compare the angular dependence of normalized bidirectional radiances as predicted by CERES *Terra* ADMs and observed by CERES over the ARM-SGP facility for selected cloud-free and overcast days. The normalized bidirectional radiance is determined from the ratio of the instantaneous radiance at a particular angle to the mean radiance from all angles observed on a given day. As shown in Figs. 8c and 8d, relative azimuth angles range from 0° to 360° and viewing zenith angles range from 25° to the limb (only viewing zenith angles out to 70° are shown). ADM-derived normalized bidirectional radiances closely track the observed values even in angles where sharp changes in the observed anisotropy occur (e.g., at relative azimuth angles near 180° in Fig. 8b). The overall error in the CERES ADM-predicted normalized radiance is $< 3\%$ for these cases.

4.2 Terra-Aqua Instantaneous TOA Flux Comparison over Greenland

While the *Terra* and *Aqua* orbits are generally well separated in time, the descending node of the *Terra* orbit does intersect with the ascending node of the *Aqua* orbit at 69.5°N, offering a unique opportunity to directly compare near-simultaneous *Terra* (FM1) and *Aqua* (FM4) TOA fluxes. Because two instruments are involved, TOA flux differences can be caused by calibration differences and ADM errors. The absolute calibration difference between FM1 and FM4 is estimated by directly comparing regionally averaged near-nadir ($\theta < 5^\circ$) radiances from the two instruments. Radiances from FM1 and FM4 acquired within 15 minutes of one another are averaged over $1^\circ \times 3^\circ$ latitude-longitude regions and directly compared. Only daytime measurements from spring and summer seasons in 2003 and 2004 over Greenland between 65°N and 75°N are considered. In the SW, the *Terra* FM1 unfiltered SW mean radiance exceeds that from *Aqua* FM4 by 1.4%. In the LW, daytime *Terra* FM1 mean radiances are smaller than FM4 by 0.8%. Similar results are obtained when separate analyses are performed for 2003 and 2004. To estimate *Terra-Aqua* TOA flux differences caused by ADM errors, the *Aqua* FM4 radiances are adjusted to account for these calibration differences prior to estimating TOA fluxes. TOA fluxes from the two instruments are compared in the same manner as the radiances, using all available viewing conditions. Only regions observed by FM1 and FM4 within 7.5 minutes are considered.

Figs. 9a-d show histograms of the relative difference between *Terra* and *Aqua* all-sky TOA fluxes for March-May (MAM) and June-August (JJA). Separate results are provided for permanent snow, fresh snow and sea-ice surface types. The overall statistics of the comparison are provided in Table 4. In the SW, *Terra* and *Aqua* TOA fluxes are within 3% of one another over permanent snow and sea-ice (MAM). In contrast, *Terra* SW TOA fluxes exceed *Aqua*

values over fresh snow (Fig. 9a) by approximately 4%, on average. In JJA, the number of fresh snow and sea-ice observations is dramatically reduced compared to MAM due to seasonal melting (Table 4). TOA flux differences over sea-ice reach 5.6% in JJA. In the LW, TOA flux differences are less than 2% in most conditions, except over fresh snow and sea-ice in JJA, when sampling is low.

4.3 Multiangle TOA Flux Consistency Tests

In Loeb et al. (2003b), regional mean TOA flux uncertainties were estimated by analyzing the consistency of instantaneous TOA fluxes estimated from near-nadir and oblique viewing angles over the same scene. More recently, Loeb et al. (2006) developed a merged dataset of CERES, Multi-Angle Imaging SpectroRadiometer (MISR) and MODIS measurements to test the self-consistency of CERES *Terra* SW TOA fluxes over ocean from up to nine coincident MISR viewing angles. Since TOA flux is independent of viewing geometry, differences between fluxes from different view angles are an indication that the anisotropy of the scene is poorly characterized by the CERES ADM. The comparisons in Loeb et al. (2003b) were limited to only 9 days of CERES *TRMM* alongtrack measurements. Here, we repeat this analysis using 124 days of CERES *Terra* alongtrack data. TOA fluxes from CERES radiances at oblique viewing zenith angles ($50^\circ < \theta < 60^\circ$) are compared with fluxes inferred from near-nadir imager radiances that have been averaged over the same footprints, after weighting by the CERES PSF. For a population of N CERES footprints, TOA flux consistency is determined from the relative root-mean-square (RMS) difference between all near-nadir and oblique view flux estimates divided by the mean TOA flux as follows:

$$\psi = \frac{\sqrt{\frac{1}{N} \sum_{i=1}^N (F(\theta_i^n) - F(\theta_i^o))^2}}{\frac{1}{N} \sum_{i=1}^N F(\theta_i^o)} \times 100\% \quad (2)$$

where $F(\theta_i^n)$ and $F(\theta_i^o)$ correspond to TOA fluxes inferred from near-nadir and oblique view angles, respectively, for the i^{th} footprint.

The imager radiances are converted to broadband radiances by applying pre-determined narrow-to-broadband radiance regressions between MODIS 0.64- μm radiances and CERES SW radiances. TOA fluxes are estimated from the “broadband” imager radiances by applying the CERES ADMs as if these radiances were actual CERES measurements.

Separate narrow-to-broadband regressions are derived each day from coincident CERES SW and MODIS 0.64- μm radiances in equal-area $1^\circ \times 1^\circ$ latitude-longitude regions using only near-nadir footprints ($\theta < 10^\circ$). To minimize narrow-to-broadband errors caused by sudden spectral changes with scene type in a $1^\circ \times 1^\circ$ latitude-longitude region, only CERES footprints belonging to the dominant scene type over the $1^\circ \times 1^\circ$ latitude-longitude region are used. Here, scene type is defined in Table 5. This classification scheme is analogous to that used by ISCCP (Rossow and Schiffer, 1999), except that an additional parameter, cloud fraction, is introduced and separate classes are provided for clear-sky and multilayer scenes. Over clear ocean, footprints influenced by strong sunglint (within 40° of the specular reflection direction) are excluded from the analysis. To produce the narrow-to-broadband fits for MODIS, near-nadir CERES crosstrack data are used in order to take advantage of the coincident CERES and MODIS viewing geometry and improved spatial coverage.

We assume that the main error sources in the CERES-MODIS TOA flux comparison are due to ADM errors and narrow-to-broadband conversion errors. The overall relative error in

radiance from the narrow-to-broadband regressions is approximately 2% in the SW and 1% in the LW. To separate the ADM errors from the total error, two comparisons are made. The first is simply the relative RMS of the difference between the near-nadir imager and oblique-view CERES TOA fluxes for a given population (e.g., a particular scene type in Table 5). One can express the total TOA flux consistency as follows:

$$\psi_1(tot)^2 = \psi_{adm}^2 + \psi_{nb}^2 \quad (3)$$

where $\psi_1(tot)$ is the total RMS TOA flux difference between near-nadir imager and oblique-view fluxes, ψ_{adm} is the RMS contribution from ADM errors, and ψ_{nb} is the RMS contribution from narrow-to-broadband errors. In the second comparison, random noise is added to the CERES radiances prior to determining the imager TOA fluxes. In that case, the total RMS error ($\psi_2(tot)$) becomes:

$$\psi_2(tot)^2 = \psi_{adm}^2 + \psi_{nb}^2 + \psi_{noise}^2 \quad (4)$$

The random noise that is added to the CERES radiances is obtained using a Gaussian random number generator with a standard deviation set by the error in the narrow-to-broadband radiance fit for each $1^\circ \times 1^\circ$ latitude-longitude region separately. Assuming the true narrow-to-broadband radiance error has a Gaussian distribution, $\psi_{noise} = \psi_{nb}$, and consequently:

$$\psi_2(tot)^2 = \psi_{adm}^2 + 2\psi_{nb}^2 \quad (5)$$

From Eq. (3)-(5), we have:

$$\psi_{adm}^2 = 2\psi_1(tot)^2 - \psi_2(tot)^2 \quad (6)$$

Because the TOA flux consistency test involves measurements from nadir and oblique viewing directions, TOA flux errors can also arise due to scene differences along the line-of-site from the two viewing directions. This may occur, for example, if clouds appear in one viewing

direction but not the other. In addition, since the two angles are collocated at the surface, the nadir and oblique viewing directions will sample different parts of a cloud because the cloud-top height is above the surface. If the cloud is spatially inhomogeneous, this can increase the RMS difference between the nadir and oblique view TOA fluxes, particularly for high clouds. This problem is mitigated when high-resolution multiangle measurements (such as MISR) are used by adjusting the reference level (i.e., the altitude where the different angles are located) to the cloud reflectance level (Moroney et al., 2002). While the problem is less severe at coarser spatial resolutions, it does add to the uncertainty in the TOA flux consistency test. No attempt is made to remove this effect in the present study.

4.3.1 Clear Ocean SW TOA Flux Consistency by Aerosol Fine-Mode Fraction

For clear ocean scenes, CERES *Terra* SW ADMs account for anisotropy changes with wind speed and aerosol optical depth (Loeb et al., 2005). However, Zhang et al. (2005) note that it may also be necessary to account for the aerosol fine-mode fraction (η) dependence in the ADMs in order to avoid introducing TOA flux biases by aerosol type. η is determined from the ratio of the fine-mode to total aerosol optical depth (Remer et al., 2005). Urban/industrial pollution and smoke from vegetation burning (mostly anthropogenic) have mostly fine (submicron) aerosol, while dust and marine aerosols (mostly natural) are dominated by coarse (supermicron) aerosol but with significant fine aerosol fraction. Since the optical properties of natural and anthropogenic aerosols are quite different (Smirnov et al., 2002), ignoring the aerosol type (or fine mode fraction) dependence may introduce errors in TOA fluxes.

To test whether or not there is any dependence in TOA flux uncertainty on η , CERES along-track TOA flux consistency tests are performed for clear ocean scenes as a function of η . To determine η , coincident retrievals of small mode and total aerosol optical depth from the

MOD04 aerosol product (Remer et al., 2005) are used. Owing to differences between the CERES and MOD04 cloud masks over ocean and other criteria for screening MOD04 retrievals (Remer et al., 2005), only 30% of the CERES footprints identified as clear ocean by the CERES cloud mask have MOD04 aerosol retrievals associated with them. Fig. 10a shows the SW TOA flux consistency between nadir and oblique view fluxes as a function of η for two intervals of solar zenith angle and aerosol optical depth (τ_a). For $\theta_o < 50^\circ$, which represents 82% of the samples (Fig. 10b), a systematic increase in the relative RMS difference of fluxes derived from nadir and oblique views with η is observed (from 3% to 6%), both at small and large aerosol optical depths. For $\theta_o > 50^\circ$, the relative RMS difference shows no dependence on η for small τ_a , whereas for $\tau_a > 0.1$ the relative RMS difference increases from 3.8% to 17.5%. Note however, that the latter represents $< 0.3\%$ of the total samples considered. Therefore, there does appear to be a systematic dependence in TOA flux uncertainty on η . Further work is needed to investigate this dependence and find optimal ways of accounting for η in future versions of the *Terra* and *Aqua* ADMs.

4.3.2 Clear Land and Desert TOA Flux Consistency by Surface Type

To account for seasonal and regional changes in SW anisotropy over land and desert, Loeb et al. (2005) use a strategy that is quite different from what has previously been used in TOA radiation budget investigations. The idea is to produce monthly $1^\circ \times 1^\circ$ latitude-longitude ADMs from parametric fits to the measurements in a manner similar to what has traditionally been used to produce bidirectional reflectance distribution functions over land using imager data (Ahmad and Deering, 1992; Wanner et al., 1997; Rahman et al., 1993). In contrast, clear land and desert ADMs for *TRMM* (Loeb et al., 2003a) were developed by grouping similar International Geosphere Biosphere Programme (IGBP) Global Land Cover types (Belward and

Loveland, 1996) together and forming four broad classes: low-to-moderate tree/shrub coverage, moderate-to-high tree/shrub coverage, dark desert, and bright desert. For snow and sea-ice, the main difference is that the *Terra* ADMs are empirical whereas the CERES *TRMM* ADMs were derived theoretically.

By applying the *TRMM* ADMs to CERES *Terra* data, the consistency of nadir and oblique view TOA fluxes using both approaches can be compared directly. Results are provided in Figs. 11a-b as a function of surface type. Fig. 11a shows the relative flux difference between the nadir and oblique views (oblique minus nadir), while Fig. 11b provides the corresponding relative RMS flux difference. Interestingly, the largest relative bias and RMS differences for the CERES *TRMM* ADMs occur for surface types that either lie predominantly at middle and high latitudes (e.g., deciduous broadleaf forest) or are represented using theoretical ADMs (e.g., permanent snow, fresh snow, sea ice). The consistency of TOA fluxes based on the *Terra* ADMs shows significant improvements compared to CERES *TRMM* ADMs. Relative biases between fluxes inferred from the nadir and oblique viewing angles remain $< 3\%$ and relative RMS differences are typically between 3% and 6%. The *Terra* relative RMS differences show notable improvements for all surface types, particularly for snow and sea-ice.

4.3.3 TOA Flux Consistency by Cloud Type

Tables 6 and 7 provide a summary of the SW and LW TOA flux relative consistency for the cloud types defined in Table 5. In the SW, the relative consistency for all scenes over ocean is 5.3%, which corresponds to 17 W m^{-2} (i.e., for conditions at *Terra* overpass times). For the most frequently occurring cloud types over ocean—low overcast clouds with moderate optical depth (cloud type 8 in Table 5) and low partly cloudy thin clouds (cloud type 1)—the TOA flux consistency is 3.5% (14 W m^{-2}) and 7.9% (8 W m^{-2}), respectively. The TOA flux consistency for mostly cloudy low-level clouds ranges from 6% to 8% ($\sim 13\text{-}17 \text{ W m}^{-2}$), and remains $< 6.5\%$ for

overcast middle and upper level clouds with moderate to thick optical depth. In general, the TOA flux consistency is $< 20 \text{ W m}^{-2}$ for low-level clouds and between 20 W m^{-2} to 30 W m^{-2} for middle and high clouds. These results are similar to those of Loeb et al. (2006) based on TOA flux consistency tests from merged CERES, MISR and MODIS measurements for up to nine coincident MISR viewing angles per footprint. Over land, the overall TOA flux consistency is the same as over ocean (5.3%). The dependence upon cloud type is also quite similar, except for low moderately thick overcast clouds, where TOA flux consistency is 8.5% over land compared to 3.5% over ocean. Consistent results over land and ocean imply that land-ocean differences in surface and cloud structure have little effect on TOA flux accuracy. In polar regions, the overall SW TOA flux relative consistency over snow and sea-ice is approximately 9% (26 W m^{-2}). The results are worse than those presented in Table 4 which compares coincident *Terra* and *Aqua* SW fluxes in the Arctic. The reason for the apparent discrepancy is because the *Terra* and *Aqua* viewing geometries for the regions compared in Table 4 are much closer together than those involved in the TOA flux consistency tests. In approximately 95% of the cases, the difference in viewing geometry between *Terra* and *Aqua* remains $< 30^\circ$, while the separation in angle in all samples considered in the TOA flux consistency test lies between 50° and 60° . RMS differences between nadir and oblique-view SW TOA fluxes in Table 6 also exceed estimates of SW TOA flux sensitivity to ADM errors in Kato and Loeb (2005). In that study, SW TOA fluxes varied by 3%-5% due to uncertainties in the ADMs, independent of any uncertainties in scene identification. Since both scene identification and ADM errors affect the results in Table 6, one expects larger differences here compared to values in Kato and Loeb (2005).

In the LW, the overall TOA flux consistency for all surfaces is $< 3\%$ ($\approx 5 - 8 \text{ W m}^{-2}$) (Table 7). A noteworthy feature in Table 7 is that the TOA flux consistency gets progressively

worse with decreasing effective cloud-top pressure. A similar dependence on effective cloud-top pressure is obtained when CERES *TRMM* ADMs are applied to the same *Terra* data. The cause for this increase is unclear. It is either due to larger ADM errors or parallax effects associated with the use of a surface reference level to collocate the nadir and oblique viewing zenith angles. Further study is needed to resolve this question.

5. Comparisons with ERBE-Like TOA Fluxes

5.1 Albedo and LW Flux Dependence on Viewing Zenith Angle

Another useful consistency test of ADMs is to stratify regional or global mean TOA fluxes by satellite viewing zenith angle. Suttles et al. (1992) used this approach to examine the consistency of TOA fluxes inferred from *Nimbus-7* Earth Radiation Budget (ERB) scanner measurements derived from ERBE ADMs (Suttles et al., 1988, 1989). They found that albedo systematically increased by 10% between nadir and $\theta=70^\circ$, and LW TOA flux decreased by 3-4%. This analysis is repeated in Figs. 12a-d using CERES *Terra* crosstrack measurements for January and July 2003. Results are shown both for global albedo and LW TOA flux inferred from the CERES ERBE-like Edition2_rev1 ES-8 and SSF Edition2_rev1 products. To determine global albedos from instantaneous TOA flux estimates, each instantaneous TOA flux is converted to a 24-hour TOA flux by applying diurnal albedo models that account for albedo changes at all times of the day, assuming the scene at the CERES *Terra* overpass time remains invariant throughout the day. The diurnal albedo models were derived from Angular Distribution Models (ADM) developed from CERES measurements on the Tropical Rainfall Measuring Mission Satellite (Loeb et al., 2003a). Similarly, instantaneous TOA fluxes from the CERES ERBE-Like ES-8 Edition2_Rev1 product are converted to 24-hour averages using diurnal albedo

models from Suttles et al. (1989). The global albedo is then determined from the ratio of the global average TOA flux to the TOA solar insolation. LW TOA fluxes are determined by averaging daytime and nighttime mean fluxes weighted by the daylight fraction of daylight in each region. SSF data are unavailable in the last viewing zenith angle bin between 65° and 70° because scene information is unavailable beyond the maximum MODIS viewing zenith angle of 63° .

Albedos based on the ERBE ADMs systematically increase by 4% and 8% with viewing zenith angle in January and July 2003, respectively (Figs. 12a and 12b). In contrast, albedos inferred from the CERES *Terra* ADMs show a smaller increase of 1%-2%. ERBE-like LW TOA fluxes show a systematic decrease with viewing zenith angle of 2%-2.4%, whereas fluxes from the CERES *Terra* ADMs remain within 0.7%-0.8% at all angles. Interestingly, ERBE-like and CERES SSF albedos are closer to one another at viewing zenith angles $< 40^\circ$, while LW fluxes are closer at viewing zenith angles $> 50^\circ$.

5.2 Monthly Mean TOA Flux Comparison

In order to compare global monthly mean TOA fluxes derived from the ERBE algorithms (Smith et al., 1986) with more recent algorithms that use the CERES *Terra* ADMs, we consider three years (March 2000 – February 2003) of CERES Level 3 data from the ERBE-like Geographical Averages (ES-4) Edition2_rev1 data product and the TOA/Surface Averages (SRBAVG) Edition2C_rev1 data product. Both of these data products provide monthly and monthly hourly regional, zonal, and globally averaged SW and LW TOA fluxes. In addition, the SRBAVG data product provides gridded SW and LW surface fluxes and cloud parameters. The ES-4 data product uses the ERBE ADMs and diurnal albedo models from Suttles et al. (1988,

1989) while the SRBAVG data product uses the CERES *Terra* ADMs and diurnal albedo models developed from CERES *TRMM* ADMs (Loeb et al., 2003a) and CERES *Terra* ADMs for snow and sea-ice (Kato and Loeb, 2005). Figs. 13a-d show ES-4 and SRBAVG global monthly mean SW and LW TOA fluxes under clear and all-sky conditions. Consistent with results shown in Figs. 12a-d, SW and LW TOA fluxes from the ES-4 product exceed fluxes in the SRBAVG product. On average, ES-4 TOA fluxes exceed SRBAVG values by 1.8 W m^{-2} and 1.3 W m^{-2} in the SW and LW, respectively. In contrast, SW clear-sky fluxes in the SRBAVG product are larger than ES-4 fluxes by 1.9 W m^{-2} , and the two are consistent to 0.4 W m^{-2} in the LW. While the seasonal cycle of TOA flux from the ES-4 and SRBAVG products are similar for all-sky conditions, they show marked differences in clear-sky conditions. SRBAVG clear-sky TOA fluxes exhibit a much smoother variation with season than ES-4 fluxes. SW TOA flux maxima in November-December and April-May appear in the SRBAVG results, but are not apparent in the ERBE-like results (Fig. 13b). These peaks are associated with higher albedos in the Antarctic and Arctic, regions where ERBE-like scene identification is poor (Li and Leighton, 1991).

Zonal differences between ES-4 and SRBAVG SW and LW TOA fluxes are shown in Figs. 14a-d for seasonal months in 2002-2003. In order to compare the two products, zonal TOA fluxes are averaged every 5° in latitude. In the SW, ES-4 fluxes are generally larger than SRBAVG fluxes at middle and high latitudes. Differences reach $6\text{-}12 \text{ W m}^{-2}$ in the northern hemisphere in April and July and in the southern hemisphere in October and January. In the tropics, SRBAVG SW TOA fluxes exceed ES-4 values by up to 3 W m^{-2} . The maximum difference generally occurs in the latitude band where the sun is closest to zenith, suggesting a solar zenith angle dependence in the ES-4 and SRBAVG SW TOA flux difference. The zonal dependence in LW TOA flux differences is far less pronounced than in the SW. In most latitude

bands ES-4 LW TOA fluxes exceed SRBAVG values by 1.0 W m^{-2} to 1.5 W m^{-2} . The zonal distribution of ES-4 and SRBAVG TOA flux differences is in stark contrast to results in Figs. 2 and 6 which show the estimated zonal error in SW and LW TOA fluxes inferred from CERES *Terra* ADMs, respectively. These results suggest that the CERES ADMs provide a significant improvement in monthly mean TOA flux accuracy compared to ERBE.

6. Summary

Recently, a new set of global ADMs based on two years of merged CERES and MODIS *Terra* measurements were developed for estimating instantaneous SW, LW and WN TOA radiative fluxes (Loeb et al., 2005). The CERES fluxes along with MODIS-derived cloud and aerosol properties and meteorological parameters from the GEOS-4 model are archived in the CERES *Terra* Single Scanner Footprint (SSF) product. The same approach has subsequently been used to develop ADMs from two years of CERES and MODIS measurements aboard the *Aqua* platform. To evaluate uncertainties in TOA fluxes derived with the CERES SW and LW ADMs, a series of consistency tests are performed. Regional monthly mean SW TOA flux uncertainties are estimated by comparing TOA fluxes generated from regional all-sky ADMs constructed using observed and CERES ADM-predicted radiances from all $10^\circ \times 10^\circ$ latitude-longitude regions over the globe. The bias in regional monthly mean SW TOA flux using this approach is less than 0.2 W m^{-2} and the regional RMS error is between 0.75 and 1.6 W m^{-2} . In contrast, SW TOA fluxes inferred using theoretical ADMs based on a plane-parallel (1D) radiative transfer model are overestimated by 3 to 4 W m^{-2} . 1D TOA regional mean flux errors also exhibit a strong latitudinal dependence that is likely due to a solar zenith angle dependent bias in the 1D model fluxes. In the LW, the bias ranges from 0.2 to 0.4 W m^{-2} , and regional RMS

errors remain smaller than 0.7 W m^{-2} for both *Terra* and *Aqua*. Bias and RMS errors in WN fluxes are approximately half as large as those in the LW.

While CERES *Terra* and CERES *Aqua* TOA flux errors are generally quite similar, differences are observed in polar regions. Biases in daytime SW TOA fluxes from *Aqua* ADMs are significantly smaller than *Terra* fluxes over sea-ice, while nighttime LW TOA flux biases over the Antarctic Plateau are smaller for *Terra*. The cause for these discrepancies is associated with differences between the *Terra* and *Aqua* CERES polar cloud mask applied to MODIS. In future editions of the SSF product, these discrepancies will be removed by applying a common cloud algorithm to both *Terra* and *Aqua*.

Uncertainties in instantaneous TOA fluxes are estimated by comparing TOA fluxes of the same scene from different viewing geometries. Based on several months of CERES alongtrack data, the SW TOA flux consistency between nadir and oblique viewing zenith angles is generally 5% over land and ocean and 9% in polar regions. When coincident *Terra* and *Aqua* SW fluxes in the Arctic are compared, TOA flux differences are generally smaller, ranging from 3% and 6%. The smaller *Terra-Aqua* TOA flux differences are due to a smaller angle separation ($< 30^\circ$) between coincident *Terra* and *Aqua* observations compared to the angle separation used in the alongtrack multiangle tests (50° - 60°). SW TOA flux differences between nadir and oblique angles over clear ocean are observed to increase with aerosol fine-mode fraction, suggesting that future versions of the CERES SW ADMs should take aerosol type into account in addition to wind speed and aerosol optical depth. Over clear land and desert, marked improvements in SW TOA flux consistency are observed using CERES *Terra* 1° regional monthly ADMs compared to CERES *TRMM* ADMs developed for just four broad classes of vegetation and types. When stratified by cloud type, the relative TOA flux consistency is typically $< 5\%$ for moderate-to-

thick low overcast scenes, and 5%-10% for broken low clouds and high clouds. In the LW, nadir and oblique view fluxes are generally consistent to 3%. Differences between nadir and oblique view fluxes show a stronger increase with cloud height than in the SW. The reason for this is unclear. It is either due to larger ADM errors or parallax effects associated with the use of a surface reference level to collocate the nadir and oblique viewing zenith angles.

When stratified by viewing zenith angle, global mean albedos derived from ADMs developed during the Earth Radiation Budget Experiment (ERBE) applied to CERES measurements systematically increase by 4% to 8% with viewing zenith angle. In contrast, albedos inferred from the CERES *Terra* ADMs show a smaller increase of 1%-2%. LW TOA fluxes from ERBE ADMs show a systematic decrease with viewing zenith angle of 2%-2.4%, whereas fluxes from the CERES *Terra* ADMs remain within 0.7%-0.8% at all angles.

Significant global and regional differences are observed when TOA fluxes from the CERES Level 3 ERBE-like Geographical Averages (ES-4) Edition2_rev1 data product and the TOA/Surface Averages (SRBAVG) Edition2C_rev1 data product are compared. On average, ES-4 TOA fluxes exceed SRBAVG values by 1.8 W m^{-2} and 1.3 W m^{-2} in the SW and LW, respectively. Clear-sky SW fluxes in the SRBAVG product are larger than ES-4 fluxes by 1.9 W m^{-2} , while the two data products are consistent to within 0.4 W m^{-2} in the LW. Zonal SW TOA flux differences reach 6-12 W m^{-2} in the northern hemisphere in April and July and in the southern hemisphere in October and January, whereas SRBAVG SW TOA fluxes exceed ES-4 values by up to 3 W m^{-2} in the tropics.

Acknowledgements

This research was funded by the Clouds and the Earth's Radiant Energy System (CERES) project under NASA grant NNL04AA26G.



References

- Ahmad, S. P., and D. W. Deering, 1992: A simple analytical function for bidirectional reflectance. *J. Geophys. Res.*, **97**, 18,867-18,886.
- Barnes, W.L., T.S. Pagano, and V.V. Salomonson, 1998: Prelaunch characteristics of the Moderate Resolution Imaging Spectroradiometer (MODIS) on EOS-AM1, *IEEE Trans. Geosci. Remote Sens.*, **36**, 1088–1100.
- Belward, A., and T. Loveland, 1996: The DIS 1km Land Cover Data Set, *GLOBAL CHANGE, The IGBP Newsletter*, #27, Sep., 1996.
- Charlock, T. P., F. G. Rose, D. A. Rutan, T. L. Alberta, D. P. Kratz, L.H. Coleman, G. L. Smith, N. Manalo-Smith, and T. D. Bess, 1997: Compute Surface and Atmospheric Fluxes (System 5.0), CERES Algorithm Theoretical Basis Document. 84 pp. [available from http://asd-www.larc.nasa.gov/ATBD/pdf_docs/r2_2/ceres-atbd2.2-s5.0.pdf].
- Geier, E.B., R. N. Green, D. P. Kratz, P. Minnis, W. F. Miller, S. K. Nolan, and C. B. Franklin, 2001: Single satellite footprint TOA/surface fluxes and clouds (SSF) collection document. [available on-line from <http://asd-www.larc.nasa.gov/CERES ASDceres.html>.]
- Ignatov, A. and L. L. Stowe, 2002: Aerosol retrievals from individual AVHRR channels: I. Retrieval algorithm and transition from Dave to 6S radiative transfer model. *J. Atm. Sci.*, **59**, 313-334.
- Kato, S., and N.G. Loeb, 2005: Top-of-atmosphere shortwave broadband observed radiance and estimated irradiance over polar regions from Clouds and the Earth's Radiant Energy System (CERES) instruments on *Terra*, *J. Geophys. Res.*, **110**, D07202, doi:10.1029/2004JD005308.



- Li., Z., and H.G. Leighton, 1991: Scene identification and its effect on cloud radiative forcing in the Arctic, *J. Geophys. Res.*, **96**, 9,175-9,188.
- Loeb, N.G., N.M. Smith, S. Kato, W.F. Miller, S.K. Gupta, P. Minnis, and B. A. Wielicki, 2003a: Angular distribution models for top-of-atmosphere radiative flux estimation from the Clouds and the Earth's Radiant Energy System instrument on the Tropical Rainfall Measuring Mission Satellite. Part I: Methodology, *J. Appl. Meteor.*, **42**, 240-265.
- Loeb, N.G., K. Loukachine, N. M. Smith, B. A. Wielicki, and D. F. Young, 2003b: Angular distribution models for top-of-atmosphere radiative flux estimation from the Clouds and the Earth's Radiant Energy System instrument on the Tropical Rainfall Measuring Mission Satellite. Part II: Validation, *J. Appl. Meteor.*, **42**, 1,748-1,769.
- Loeb, N.G., S. Kato, K. Loukachine, and N. Manalo-Smith, 2005: Angular distribution models for top-of-atmosphere radiative flux estimation from the Clouds and the Earth's Radiant Energy System instrument on the *Terra* Satellite. Part I: Methodology. *J. Atmos. Ocean. Tech.*, **22**, 338-351.
- Loeb, N.G., and N. Manalo-Smith, 2005: Top-of-atmosphere direct radiative effect of aerosols over global oceans from merged CERES and MODIS observations, *J. Climate*, **18**, 3506-3526.
- Loeb, N. G., W. Sun, W. F. Miller, K. Loukachine, and R. Davies, 2006: Fusion of CERES, MISR and MODIS measurements for top-of-atmosphere radiative flux validation, *J. Geophys. Res.* (submitted).

- Loeb, N.G., and J.A. Coakley, Jr., 1998: Inference of marine stratus cloud optical depths from satellite measurements: Does 1D theory apply? *J. Climate*, **11**, 215-233.
- Loeb, N.G., and R. Davies, 1996: Observational evidence of plane parallel model biases: The apparent dependence of cloud optical depth on solar zenith angle. *J. Geophys. Res.*, **101**, 1621-1634.
- Minnis, P., D. P. Garber, D. F. Young, R. F. Arduini, and Y. Tokano, 1998: Parameterizations of reflectance and effective emittance for satellite remote sensing of cloud properties. *J. Atmos. Sci.*, **55**, 3313-3339.
- Minnis, P., D. F. Young, S. Sun-Mack, P. W. Heck, D. R. Doelling, and Q. Trepte, 2003: CERES Cloud Property Retrievals from Imagers on TRMM, Terra, and Aqua, *Proc. SPIE 10th International Symposium on Remote Sensing: Conference on Remote Sensing of Clouds and the Atmosphere VII*, Barcelona, Spain, September 8-12, 37-48.
- Moroney, C., Horvath, A. and Roger Davies, 2002: Use of stereo-matching to coregister multiangle data from MISR. *IEEE Trans. Geosci. Remote Sens.*, **40**, 1541-1546.
- Nakajima, T., and M. Tanaka, 1986: Matrix formulations for the transfer of solar radiation in a plane-parallel scattering atmosphere. *J. Quant. Spectrosc. Radiat. Transfer*, **35**, 13-21.
- Nakajima, T., and M. Tanaka, 1988: Algorithms for radiative intensity calculations in moderately thick atmospheres using a truncation approximation. *J. Quant. Spectrosc. Radiat. Transfer*, **40**, 51-69.
- Rahman, H., M.M. Verstraete, and B. Pinty, 1993: Coupled surface-atmosphere reflectance (CSAR) model 1. Model description and inversion on synthetic data. *J. Geophys. Res.*, **98**, 20,779-20,789.



- Remer, L. A., Y. J. Kaufman, D. Tanré, S. Mattoo, D. A. Chu, J. V. Martins, R-R. Li, C. Ichoku, R. C. Levy, R. G. Kleidman, T. F. Eck, E. Vermote, and B. N. Holben (2005), The MODIS Aerosol Algorithm, Products and Validation, *J. Atmos. Sci.*, **62**, 947-973.
- Rossow, W.B., and R.A. Schiffer, 1999: Advances in understanding clouds from ISCCP, *Bull. Amer. Meteor. Soc.*, **80**, 2261-2287.
- Smirnov, A., B.N. Holben, Y.J. Kaufman, et al., 2002: Optical properties of atmospheric aerosol in maritime environments, *J. Atmos. Sci.*, **59**, 501-523.
- Smith, G. L., R. N. Green, E. Raschke, L. M. Avis, J. T. Suttles, B. A. Wielicki, and R. Davies, 1986: Inversion methods for satellite studies of the earth radiation budget: Development of algorithms for the ERBE mission. *Rev. Geophys.*, **24**, 407-421.
- Suarez, M. J. (2005), Technical report series on global modeling and data assimilation, Vol. 26: Documentation and validation of the Goddard Earth Observing System (GEOS) data assimilation system—Version 4, NASA/TM—2005—104606, Vol. 26, 181 pp., Washington, DC.
- Suttles, J.T., B.A. Wielicki, and S. Vemury, 1992: Top-of-atmosphere radiative fluxes: Validation of ERBE scanner inversion algorithm using Nimbus-7 ERB data. *J. Appl. Meteor.*, **31**, 784-796.
- Suttles, J.T., R.N. Green, P. Minnis, G.L. Smith, W.F. Staylor, B.A. Wielicki, I.J. Walker, D.E. Young, V.R. Taylor, and L.L. Stowe, 1988: Angular radiation models for Earth-atmosphere systems, Vol. I—shortwave radiation. *Rep. NASA RP-1184*, NASA, Washington, D.C.
- Suttles, J.T., R.N. Green, G.L. Smith, B.A. Wielicki, I.J. Walker, V.R. Taylor, and L.L. Stowe, 1989: Angular radiation models for Earth-atmosphere systems, Vol. II—longwave radiation. *Rep. NASA RP-1184*, NASA, Washington, D.C.



- Wanner, W., A.H. Strahler, B. Hu, P. Lewis, J.-P. Muller, X. Li, C. L. Barker Schaaf, and M. J. Barnsley, 1997: Global retrieval of bidirectional reflectance and albedo over land from EOS MODIS and MISR data: Theory and algorithm, *J. Geophys. Res.*, **102**, 17,143–17,162.
- Wielicki, B. A., B. R. Barkstrom, E. F. Harrison, R. B. Lee III, G. L. Smith, and J. E. Cooper, 1996: Clouds and the Earth's Radiant Energy System (CERES): An Earth observing system experiment. *Bull. Amer. Meteorol. Soc.*, **77**, 853-868.
- Wielicki, B.A., R. D. Cess, M. D. King, D. A. Randall, and E. F. Harrison, 1995: Mission to planet Earth: Role of clouds and radiation in climate. *Bull. Amer. Meteor. Soc.*, **76**, 2125-2152.
- Zhang, J., S.A. Christopher, L.A. Remer, Y. Kaufman, 2005: Shortwave aerosol radiative forcing over cloud-free oceans from *Terra*: 1. Angular models for aerosols, *J. Geophys. Res.*, **110**, D10S23, doi:10.1029/2004JD005008.

Figures

Figure 1 Error in regional mean SW TOA flux due to ADM uncertainties for (a) January, (b) April, (c) July and (d) October.

Figure 2 *Terra* and Aqua regional SW TOA flux error due to ADM uncertainties for (a) January, (b) April, (c) July and (d) October 2003.

Figure 3 Regional SW TOA flux error for July 2003 from *Terra* and Aqua ADMs using CERES cloud retrievals from (a) *Terra* and (b) Aqua for scene identification.

Figure 4 Error in regional mean SW TOA flux for liquid water clouds over ice-free ocean due to ADM uncertainties for (a) July and (b) January using 1D ADMs; (c) July and (d) January using CERES *Terra* ADMs.

Figure 5 24-hour average regional LW TOA flux error due to ADM uncertainties for (a) January, (b) April, (c) July and (d) October.

Figure 6 *Terra* and Aqua regional LW TOA flux error due to ADM uncertainties for (a) January, (b) April, (c) July and (d) October 2003.

Figure 7 Nighttime LW TOA flux error against viewing zenith angle for (a) Aqua and (b) *Terra* in three Antarctic regions in October 2003.

Figure 8 Estimated and observed instantaneous normalized SW radiance against relative azimuth angle for (a) cloud-free and (b) overcast days over the ARM-SGP site in May 2003 when the CERES FM2 instrument was in PAP mode. Figs. 8c and 8d provide the solar and viewing zenith angles corresponding to Figs. 8a and 8b, respectively.

Figure 9 Histogram of relative difference between matched CERES *Terra* and Aqua $1^{\circ} \times 3^{\circ}$ regional daily mean instantaneous SW (9a and 9c) and LW (9b and 9d) TOA fluxes for March-May, 2004 (9a and 9b) and June-August 2003 (9c and 9d).

Figure 10 (a) SW TOA flux consistency as a function of fine-mode-fraction for two intervals of solar zenith angle and aerosol optical depth (τ_a). (b) Relative frequency of occurrence of each θ_o and τ_a interval in Fig. 10a. A total of 23,601 footprints are considered.

Figure 11 Clear-sky multiangle SW TOA flux consistency: (a) relative difference $[F(\theta=50^\circ-60^\circ) - F(\text{Nadir})] / F(\text{Nadir}) \times 100\%$; (b) relative RMS difference.

Figure 12 SSF and ES8 global albedo against viewing zenith angle for (a) January and (b) July 2003. LW TOA flux against viewing zenith angle for (c) January and (d) July 2003.

Figure 13 Global TOA flux derived from SRBAVG and ES4 products for (a) all-sky SW; (b) clear-sky SW; (c) all-sky LW; (d) clear-sky LW.

Figure 14 SW and LW TOA flux differences between the ES-4 and SRBAVG products for (a) April 2002; (b) July 2002; (c) October 2002; (d) January 2003. Zonal fluxes in both products were averaged to a common 5° latitude increment.

Tables

Season	<i>Aqua</i>		<i>Terra</i>	
	Bias (W m^{-2})	RMS (W m^{-2})	Bias (W m^{-2})	RMS (W m^{-2})
January	0.13	0.75	0.11	0.98
April	-0.16	0.70	0.00	0.99
July	-0.02	1.08	0.02	1.37
October	-0.10	0.68	0.11	0.76

Table 1 Regional mean SW TOA flux bias and RMS error for *Aqua* and *Terra* by season for December 2002 – November 2003.

Season	<i>Aqua</i>		<i>Terra</i>	
	Bias (W m-2)	RMS (W m-2)	Bias (W m-2)	RMS (W m-2)
January	0.26	0.51	0.17	0.57
April	0.31	0.58	0.35	0.66
July	0.25	0.56	0.33	0.63
October	0.22	0.55	0.27	0.58

Table 2 Regional mean LW TOA flux bias and RMS error for *Aqua* and *Terra* by season for December 2002 – November 2003.

	<i>Aqua</i>		<i>Terra</i>	
	Bias (W m-2)	RMS (W m-2)	Bias (W m-2)	RMS (W m-2)
January	0.16	0.24	0.17	0.28
April	0.19	0.27	0.23	0.34
July	0.17	0.27	0.22	0.32
October	0.16	0.25	0.20	0.29

Table 3 Regional mean WN TOA flux bias and RMS error for *Aqua* and *Terra* by season for December 2002 – November 2003.

	<i>N</i>	SW		LW	
		Rel. Diff. (%)	Rel. RMS Diff. (%)	Rel. Diff. (%)	Rel. RMS Diff. (%)
Permanent Snow (MAM)	1609	0.5	1.5	-1.4	1.7
Fresh Snow (MAM)	7676	3.6	4.4	-1.2	1.5
Sea Ice (MAM)	3545	1.0	2.3	-1.1	1.4
Permanent Snow (JJA)	1360	0.06	2.5	-0.12	1.3
Fresh Snow (JJA)	120	-1.6	6.5	2.6	3.3
Sea Ice (JJA)	662	-2.4	5.6	1.3	2.3

Table 4 Relative difference and relative RMS difference between matched regional daily mean instantaneous TOA fluxes from CERES *Terra* and *Aqua* for MAM, 2004 and JJA, 2003. *N* is the number of 1°x3° regional daily mean fluxes.

	PCL			MCL			OVC			Clear	Multi-layer												
High	19	20	21	22	23	24	25	26	27	28	29												
Middle	10	11	12	13	14	15	16	17	18														
Low	1	2	3	4	5	6	7	8	9														
	Thin	Mod	Thk	Thin	Mod	Thk	Thin	Mod	Thk														
<table border="1"> <tr> <td>Clear: $f \leq 0.001$</td> <td>High: $p_t < 440$ mb</td> <td>Thin: $e^{\langle \ln \tau \rangle} \leq 3.35$</td> <td rowspan="4">Multilayer: Two distinct cloud layers in CERES footprint</td> </tr> <tr> <td>PCL: $0.001 < f \leq 0.4$</td> <td>Middle: $440 \text{ mb} \leq p_t < 680$ mb</td> <td>Mod: $3.35 < e^{\langle \ln \tau \rangle} \leq 22.63$</td> </tr> <tr> <td>MCL: $0.4 < f \leq 0.99$</td> <td>Low: $p_t \geq 680$ mb</td> <td>Thk: $e^{\langle \ln \tau \rangle} > 22.63$</td> </tr> <tr> <td>OVC: $0.99 < f \leq 1.0$</td> <td></td> <td></td> </tr> </table>											Clear: $f \leq 0.001$	High: $p_t < 440$ mb	Thin: $e^{\langle \ln \tau \rangle} \leq 3.35$	Multilayer: Two distinct cloud layers in CERES footprint	PCL: $0.001 < f \leq 0.4$	Middle: $440 \text{ mb} \leq p_t < 680$ mb	Mod: $3.35 < e^{\langle \ln \tau \rangle} \leq 22.63$	MCL: $0.4 < f \leq 0.99$	Low: $p_t \geq 680$ mb	Thk: $e^{\langle \ln \tau \rangle} > 22.63$	OVC: $0.99 < f \leq 1.0$		
Clear: $f \leq 0.001$	High: $p_t < 440$ mb	Thin: $e^{\langle \ln \tau \rangle} \leq 3.35$	Multilayer: Two distinct cloud layers in CERES footprint																				
PCL: $0.001 < f \leq 0.4$	Middle: $440 \text{ mb} \leq p_t < 680$ mb	Mod: $3.35 < e^{\langle \ln \tau \rangle} \leq 22.63$																					
MCL: $0.4 < f \leq 0.99$	Low: $p_t \geq 680$ mb	Thk: $e^{\langle \ln \tau \rangle} > 22.63$																					
OVC: $0.99 < f \leq 1.0$																							

Table 5 Scene type classification scheme used in multiangle TOA flux consistency tests. Each CERES footprint is assigned a scene identification index from 1 through 29 based on the cloud fraction (f), mean effective cloud-top pressure (p_t), cloud optical depth ($e^{\langle \ln \tau \rangle}$), and whether one or two cloud layers are observed within the footprint.

Ocean											
	PCL			MCL			OVC			Clear	Multi-Layer
High	17			11			11	6.5	3.9	4.6	11
Middle							9.7	5.4	4.5	All-Sky	
Low	7.9	10		8.0	6.0			3.5	4.2	5.3	
	Thin	Mod	Thk	Thin	Mod	Thk	Thin	Mod	Thk		
Land/Desert											
	PCL			MCL			OVC			Clear	Multi-Layer
High	6.4						18	6.4	4.3	4.5	6.3
Middle	3.3				9.4			4.8	4.6	All-Sky	
Low	8.1	6.8		6.2	5.5			8.5	4.3	5.3	
	Thin	Mod	Thk	Thin	Mod	Thk	Thin	Mod	Thk		
Snow/Sea-Ice											
	PCL			MCL			OVC			Clear	Multi-Layer
High							9.6	6.4	10	8.0	9.8
Middle	8.8	24		8.2			8.6	4.7	17	All-Sky	
Low	12	19		11	11		14	6.1	6.4	8.9	
	Thin	Mod	Thk	Thin	Mod	Thk	Thin	Mod	Thk		

Table 6 SW TOA flux consistency (%) (defined in Eq. (2)) for ocean, land/desert and Snow/Sea-Ice by cloud type. Only cloud types with at least 100 footprints are considered.

Ocean											
	PCL			MCL			OVC			Clear	Multi-Layer
High	2.6			5.4			7.4	8.4	7.2	1.2	3.2
Middle							4.5	4.7	4.3	All-Sky	
Low	1.3	1.3		1.7	2.5		2.5	2.7	2.7	2.9	
	Thin	Mod	Thk	Thin	Mod	Thk	Thin	Mod	Thk		
Land/Desert											
	PCL			MCL			OVC			Clear	Multi-Layer
High	6.6						7.6	8.4	7.1	2.3	2.9
Middle	3.3	2.6			3.7			4.3	3.8	All-Sky	
Low	2.3	2.2		2.7	2.4			2.3	2.6	2.6	
	Thin	Mod	Thk	Thin	Mod	Thk	Thin	Mod	Thk		
Snow/Sea-Ice											
	PCL			MCL			OVC			Clear	Multi-Layer
High							5.3	5.0	4.2	2.9	3.4
Middle	3.7	6.1		2.4			4.9	4.9	5.6	All-Sky	
Low	2.6	1.3		2.4	2.3		4.0	2.4	4.7	2.9	
	Thin	Mod	Thk	Thin	Mod	Thk	Thin	Mod	Thk		

Table 7 LW TOA flux consistency (%) for ocean, land/desert and Snow/Sea-Ice by cloud type. Only cloud types with at least 100 footprints are considered.

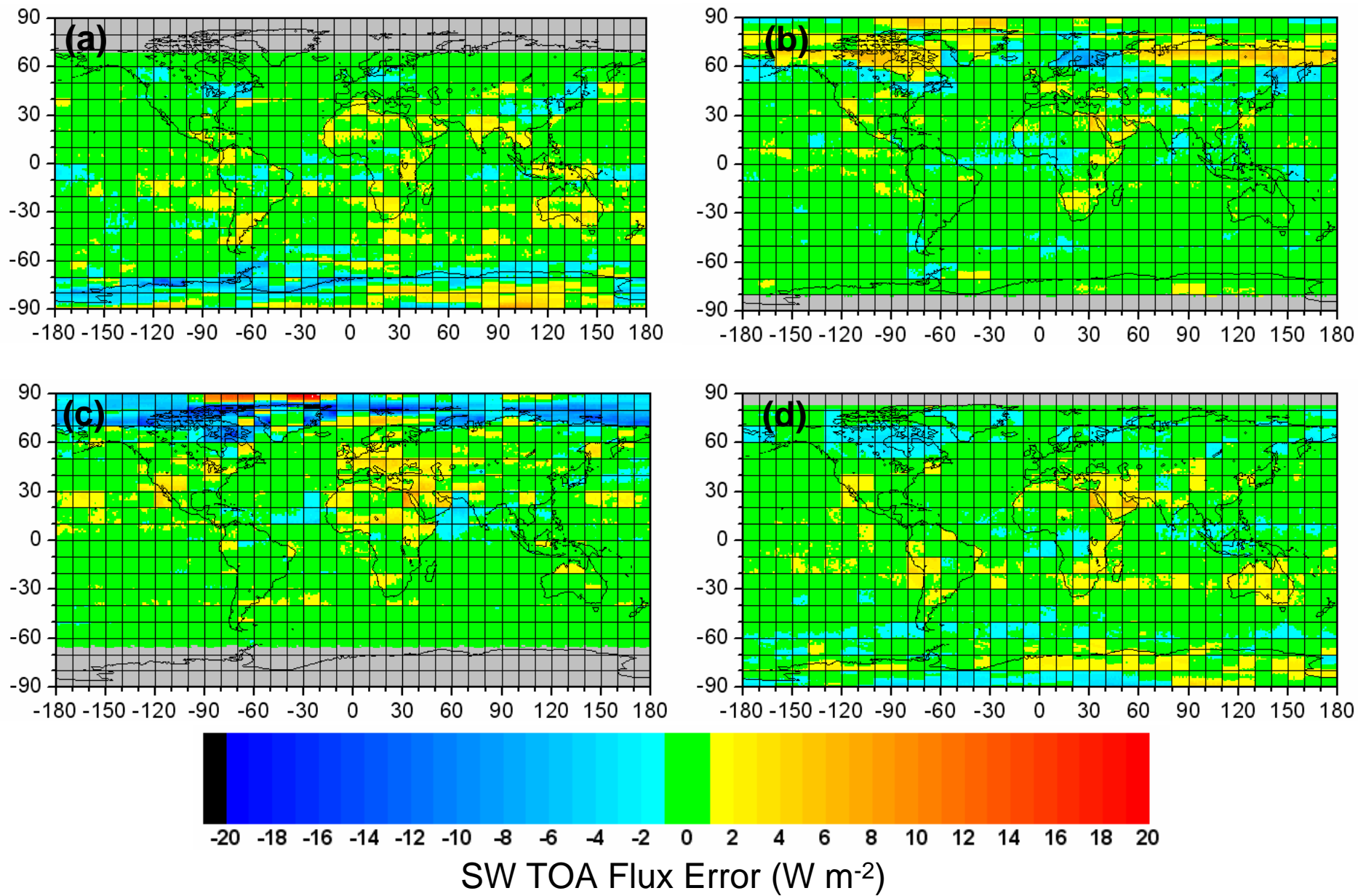


Figure 1 Error in regional mean SW TOA flux due to ADM uncertainties for (a) January, (b) April, (c) July and (d) October 2003.

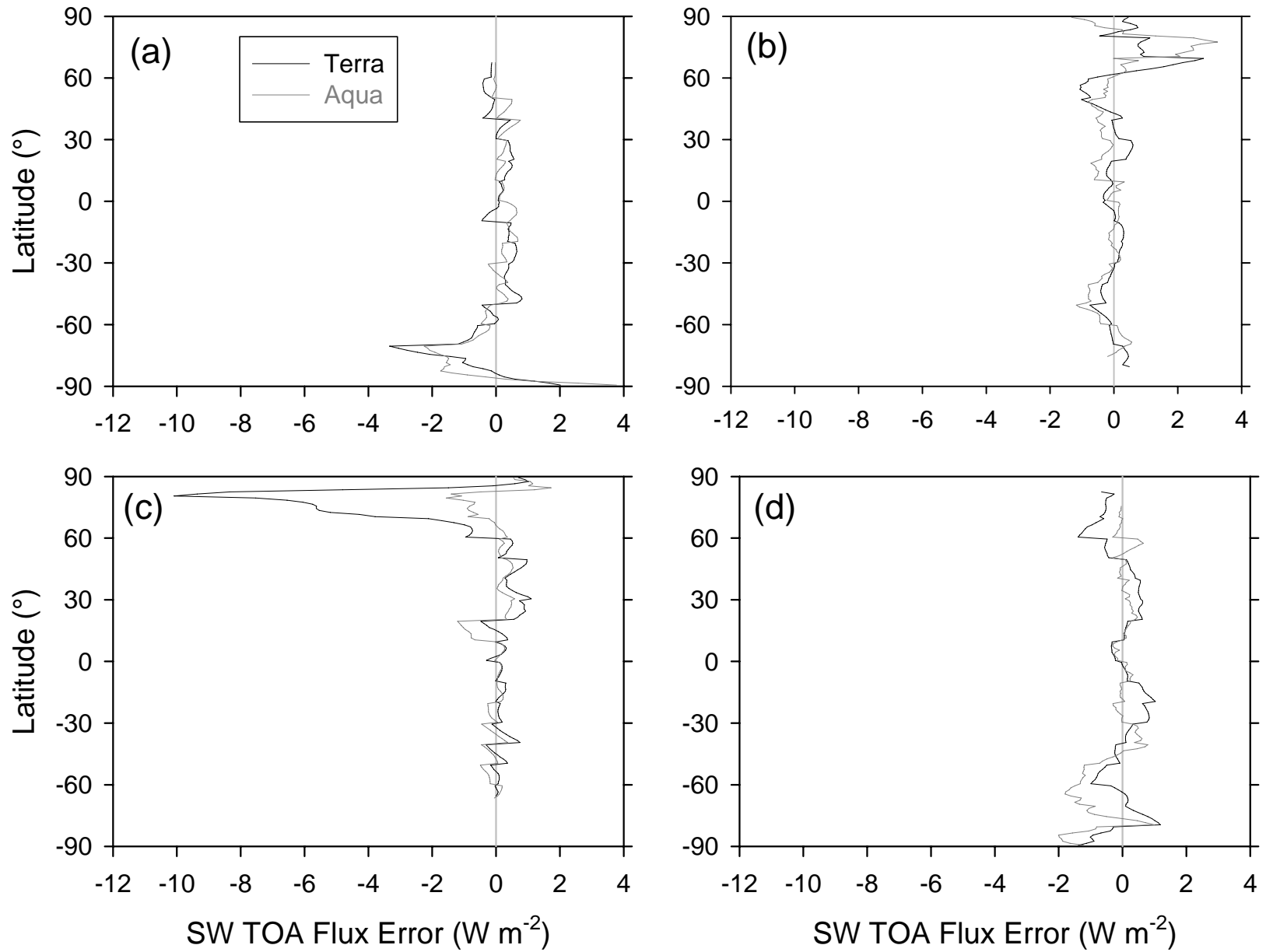


Figure 2 Terra and Aqua regional SW TOA flux error due to ADM uncertainties for (a) January, (b) April, (c) July and (d) October 2003.

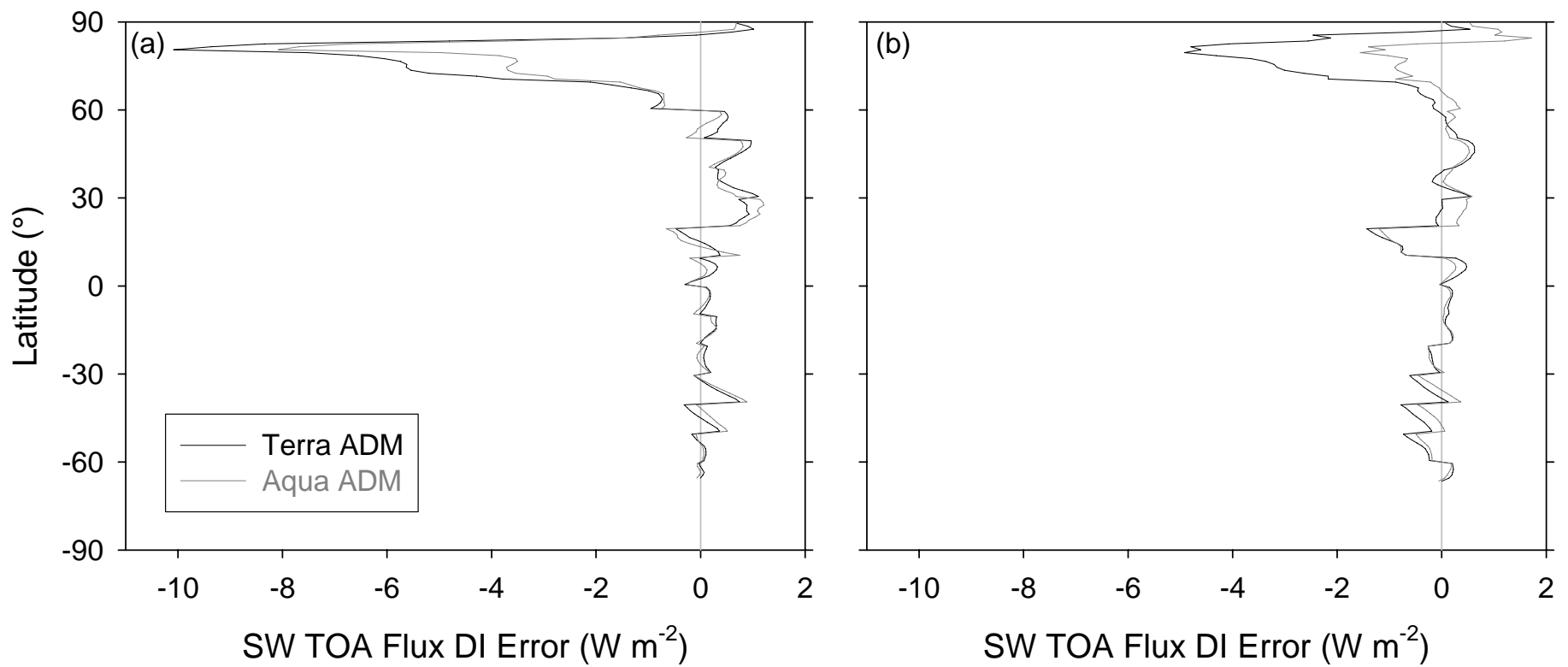


Figure 3 Regional SW TOA flux error for July 2003 from Terra and Aqua ADMs using CERES cloud retrievals from (a) Terra and (b) Aqua for scene identification.



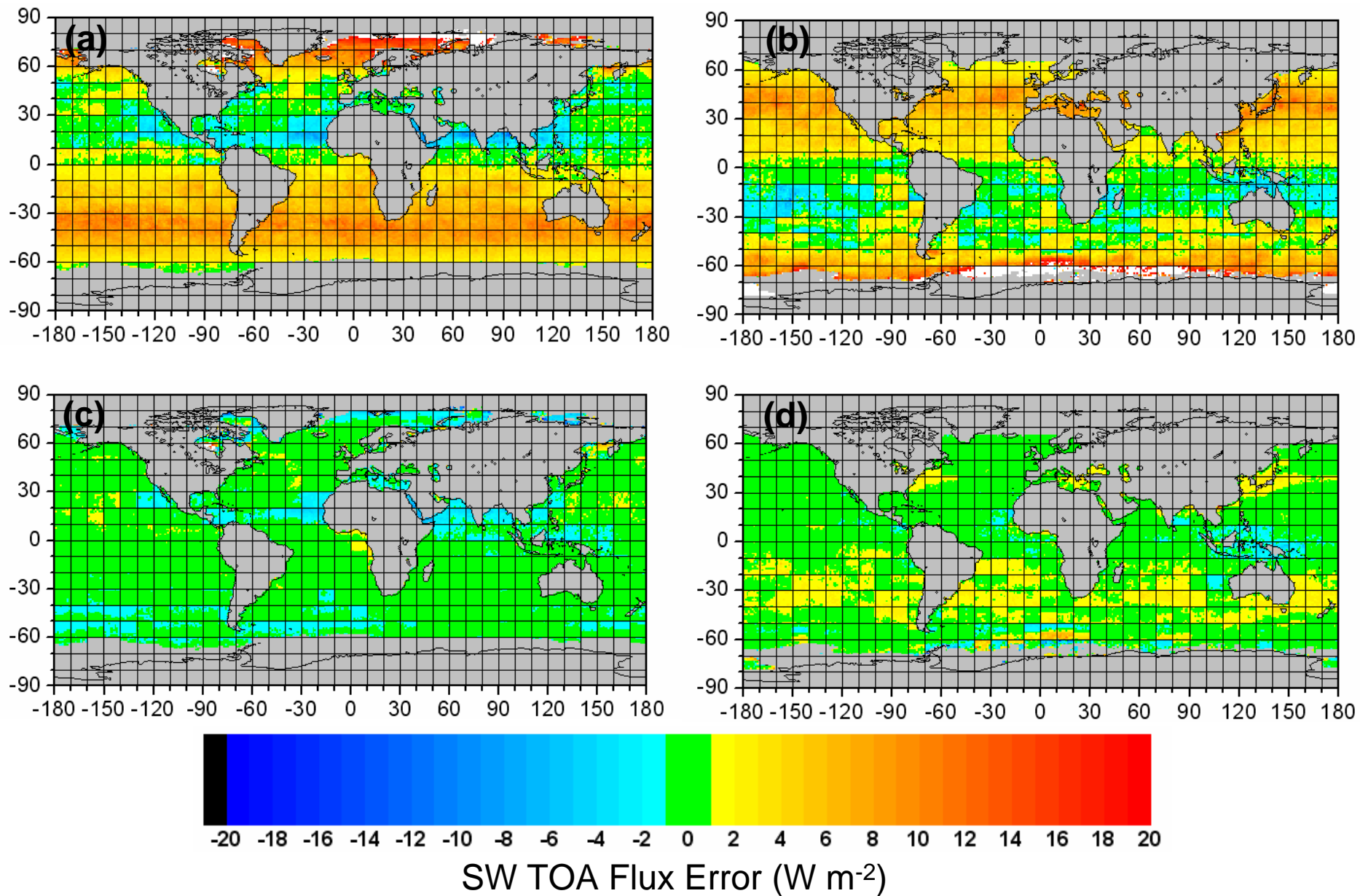
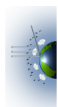


Figure 4 Error in regional mean SW TOA flux for liquid water clouds over ice-free ocean due to ADM uncertainties for (a) July and (b) January using 1D ADMs; (c) July and (d) January using CERES Terra ADMs.



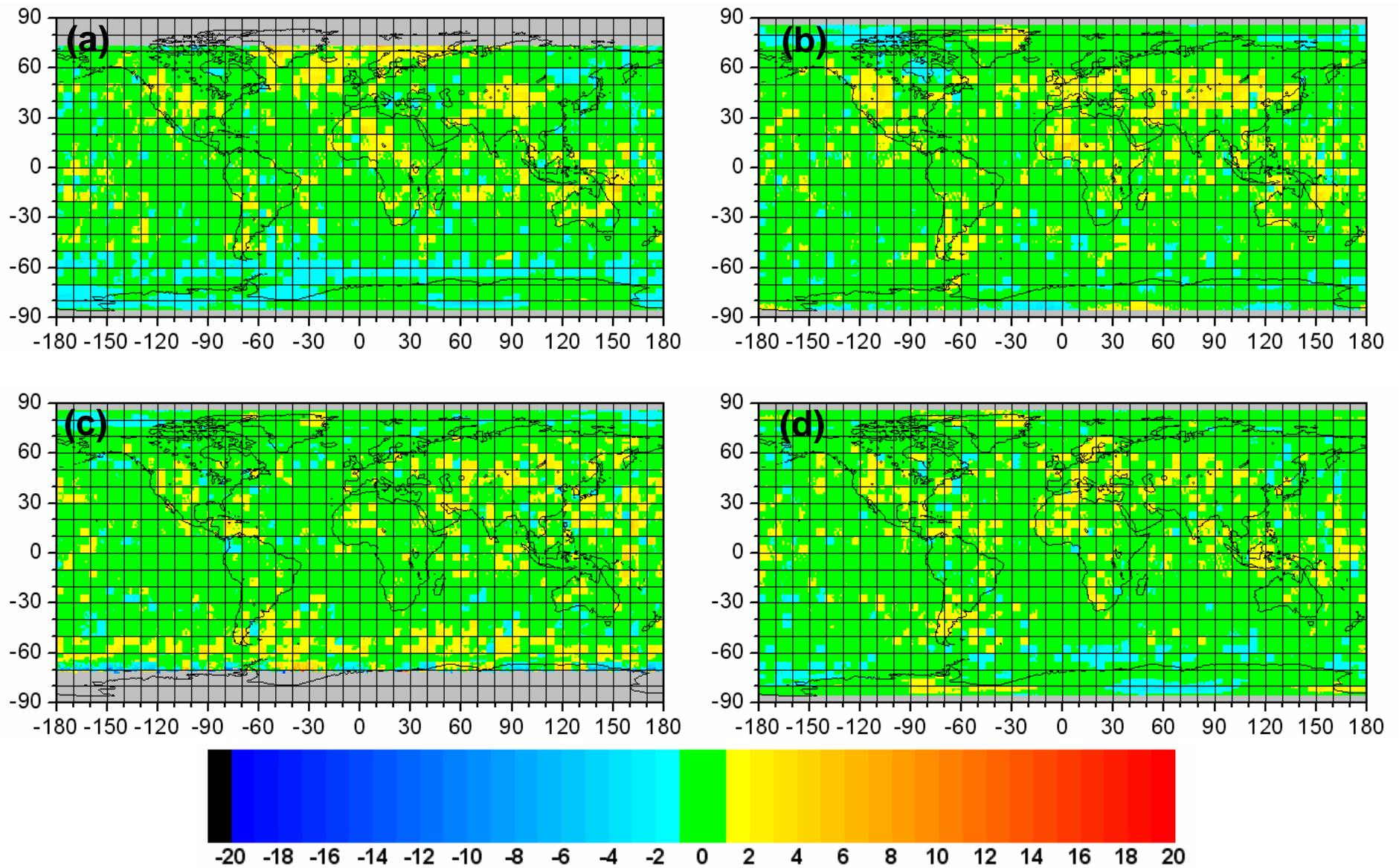


Figure 5 24-hour average regional LW TOA flux error due to ADM uncertainties for (a) January, (b) April, (c) July and (d) October 2003.



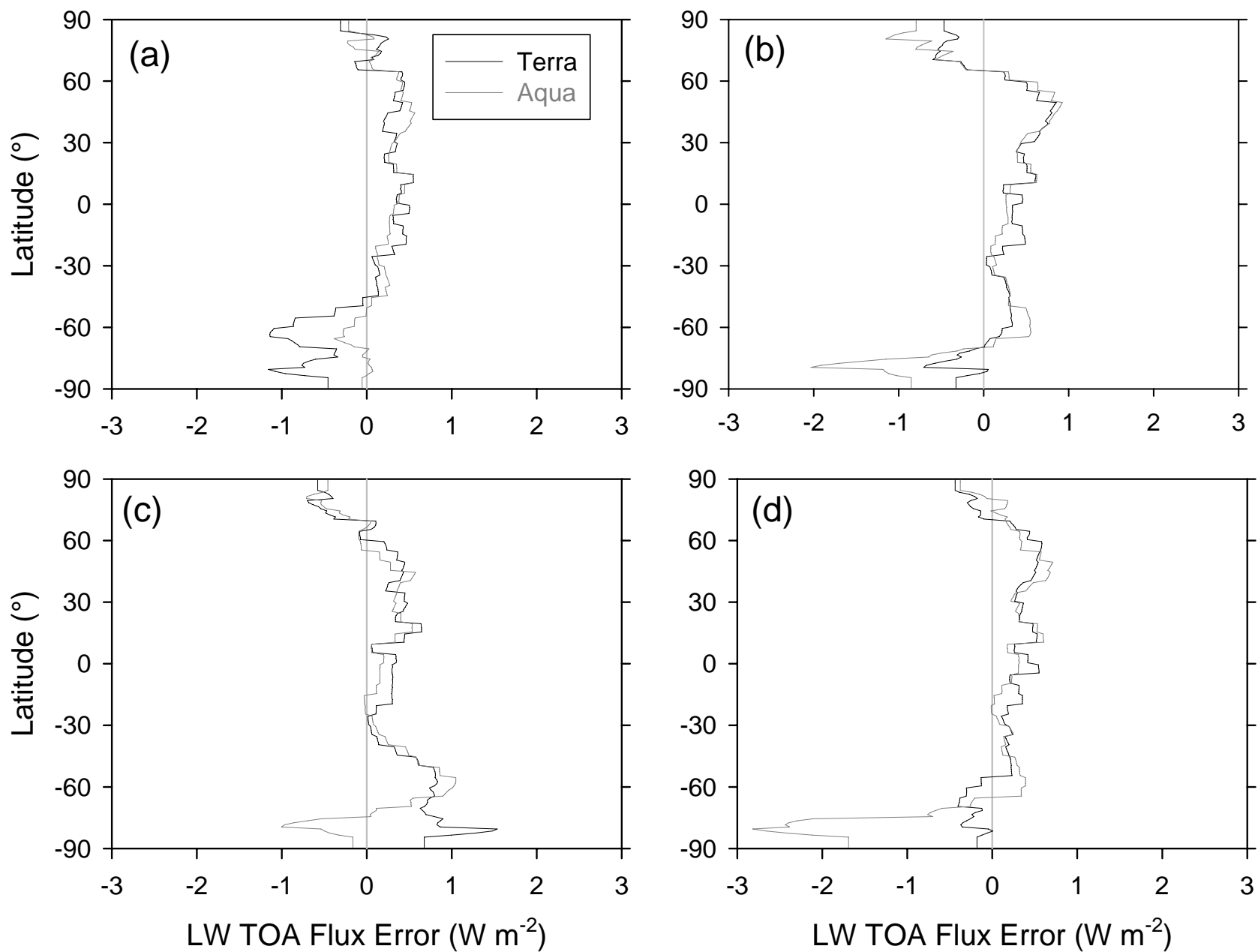


Figure 6 Terra and Aqua regional LW TOA flux error due to ADM uncertainties for (a) January, (b) April, (c) July and (d) October 2003

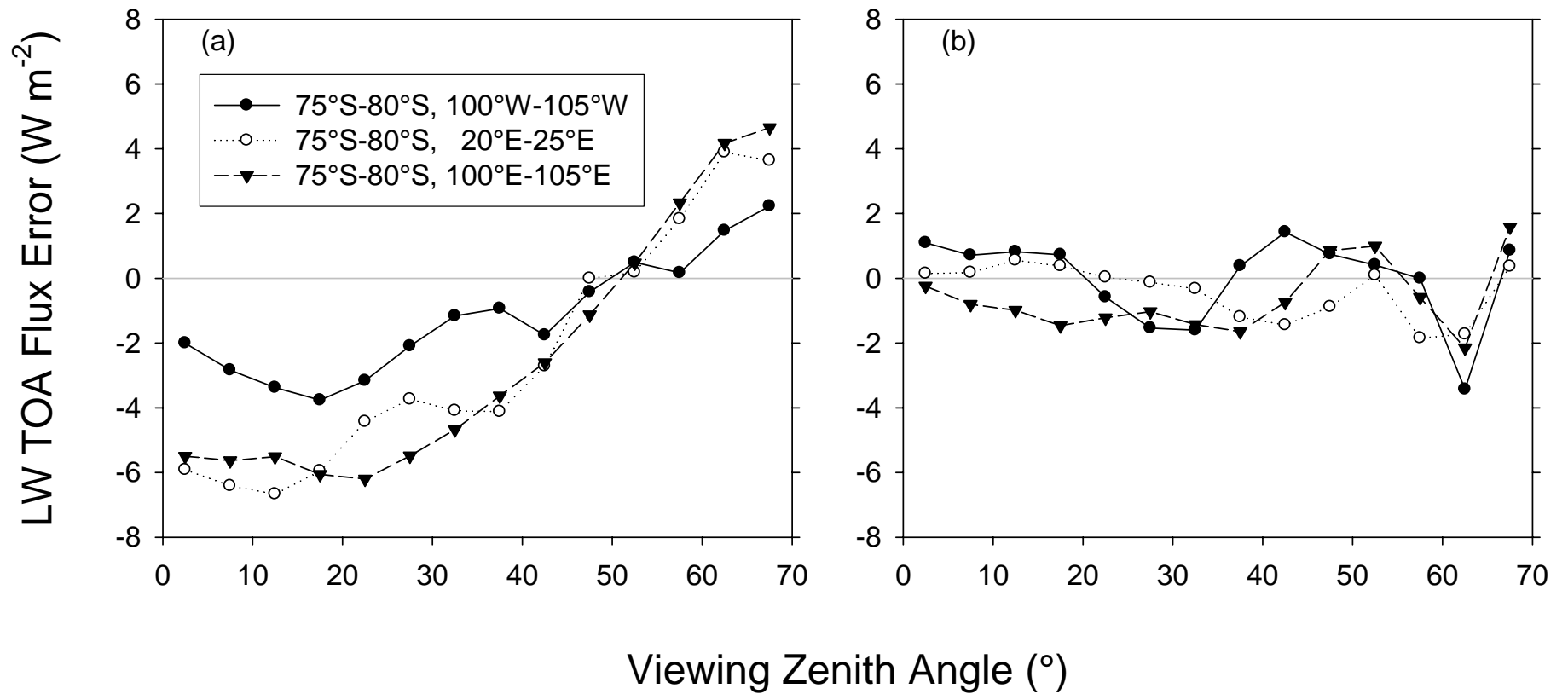


Figure 7 Nighttime LW TOA flux error against viewing zenith angle for (a) Aqua and (b) Terra in three Antarctic regions in October 2003.

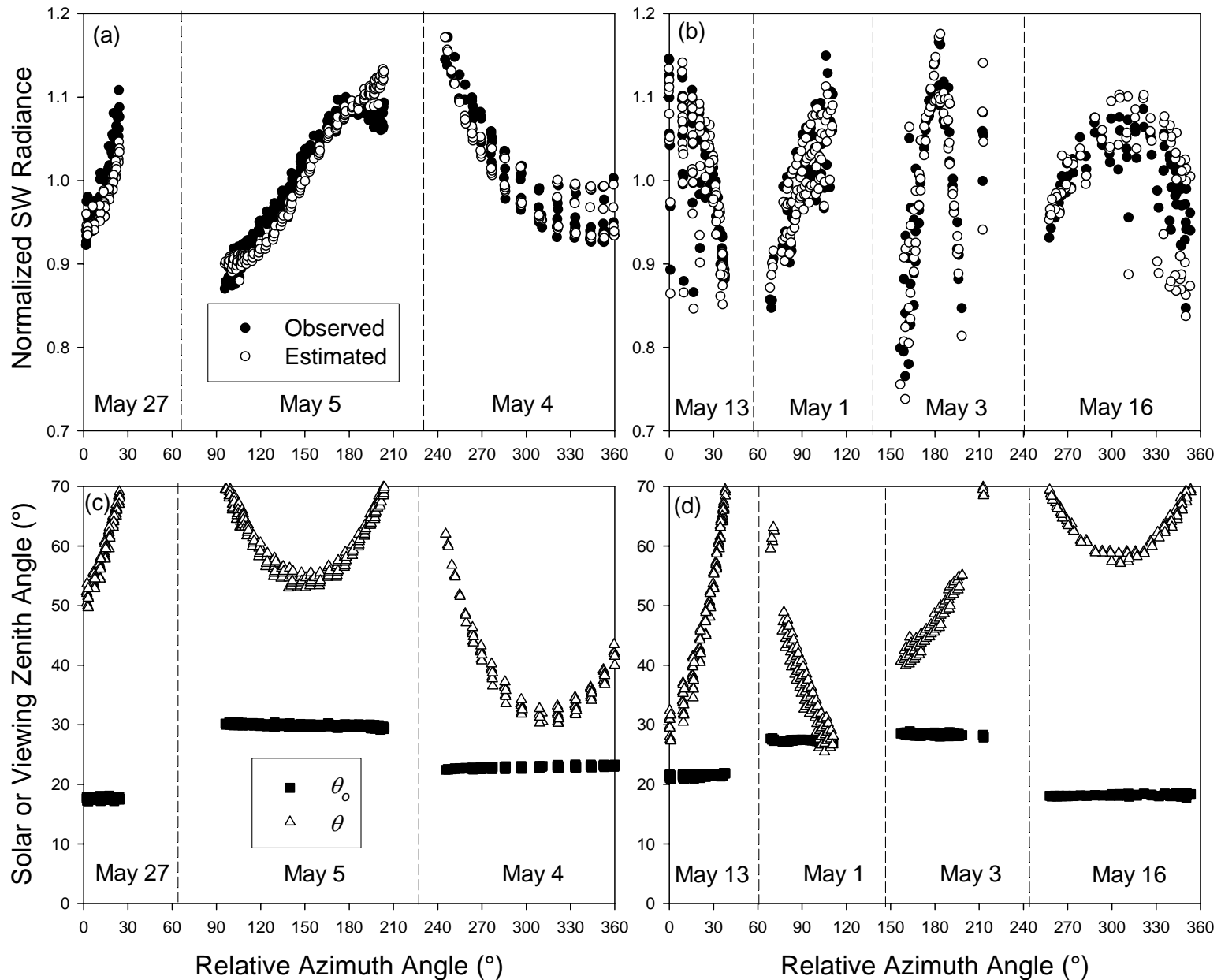


Figure 8 Estimated and observed instantaneous normalized SW radiance against relative azimuth angle for (a) cloud-free and (b) overcast days over the ARM SGP site in May 2003 when the CERES FM2 instrument was in PAP mode. Figs. 8c and 8d provide the solar and viewing zenith angles corresponding to Figs. 8a and 8b, respectively.

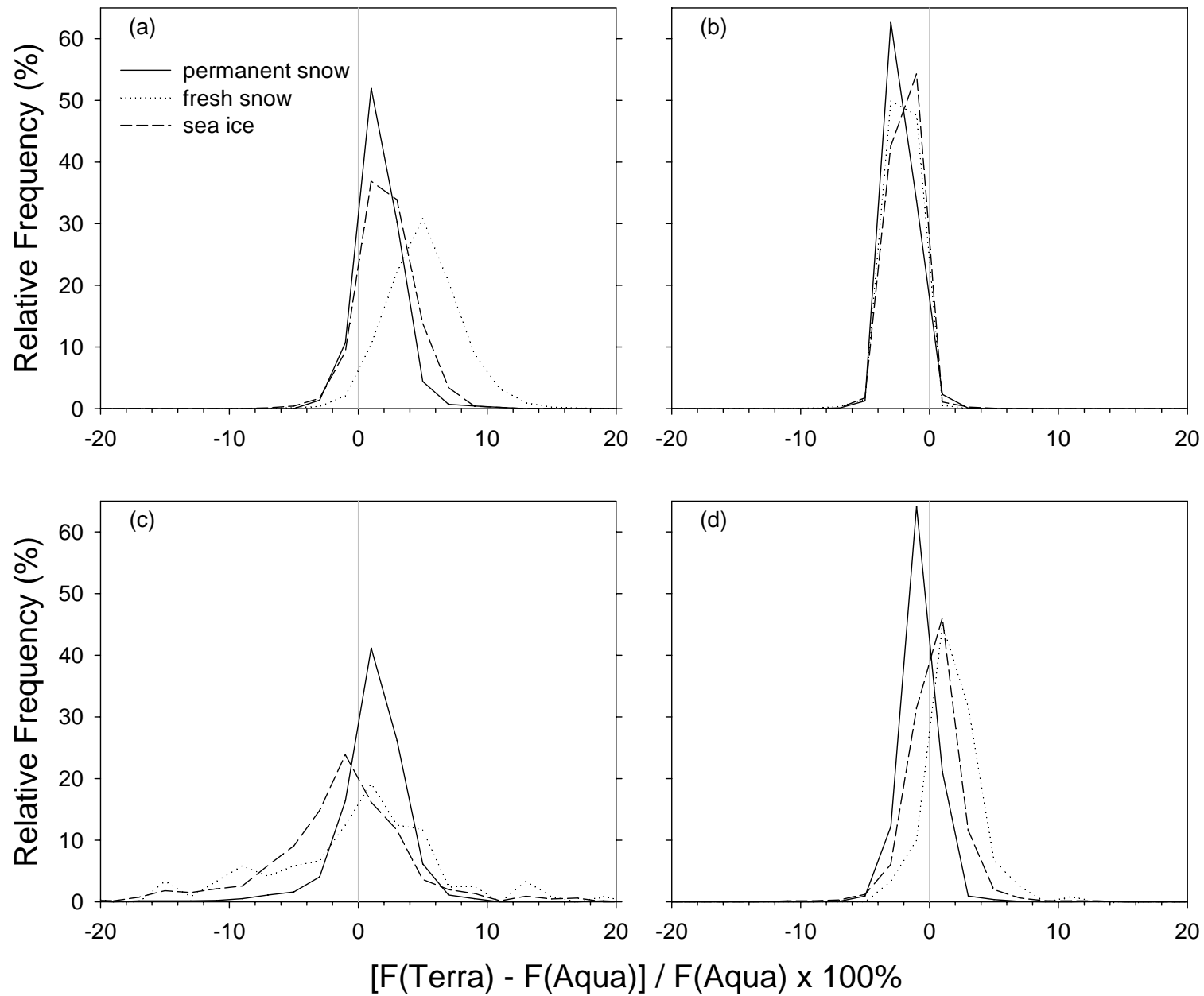
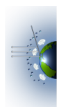
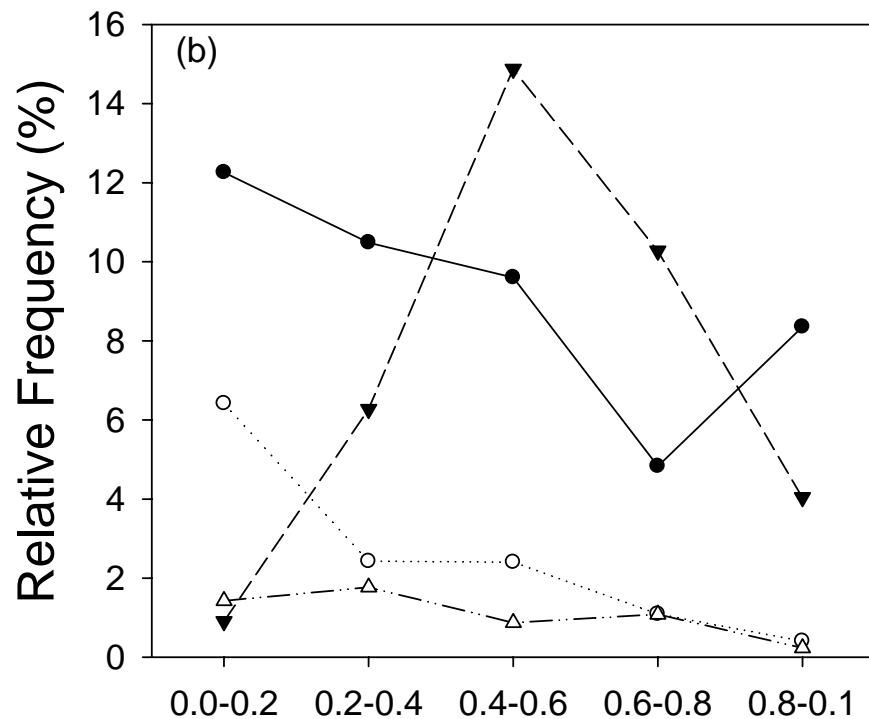
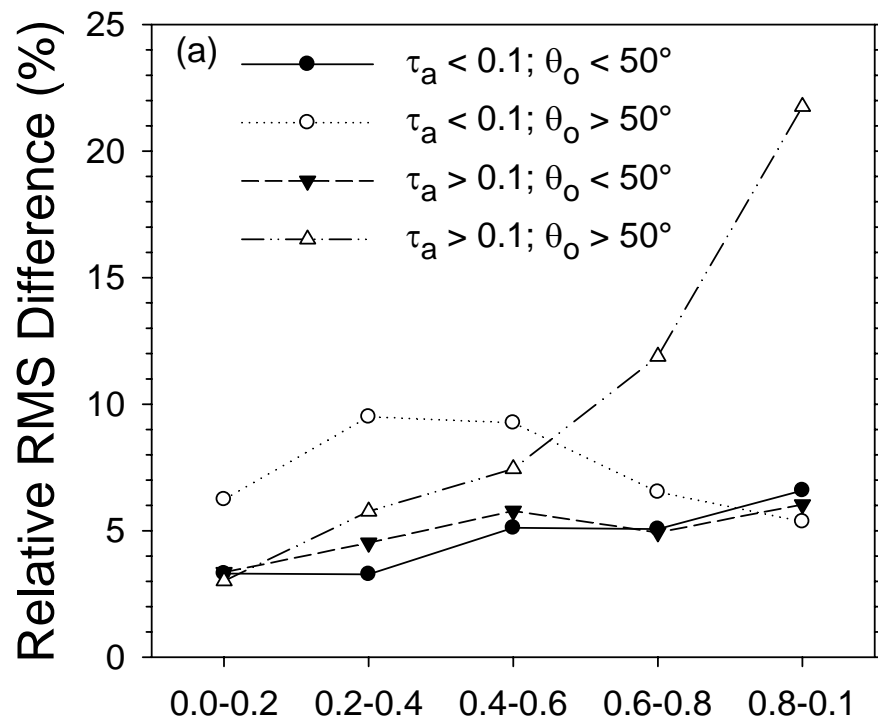


Figure 9 Histogram of relative difference between matched CERES Terra and Aqua $1^\circ \times 3^\circ$ regional daily mean instantaneous SW (9a and 9c) and LW (9b and 9d) TOA fluxes for March-May, 2004 (9a and 9b) and June-August 2003 (9c and 9d).





0.55 μm Aerosol Fine Mode Fraction

Figure 10 (a) SW TOA flux consistency as a function of fine-mode-fraction for two intervals of solar zenith angle and aerosol optical depth (τ_a). (b) Relative frequency of occurrence of each θ_o and τ_a interval in Fig. 10a. A total of 23,601 footprints are considered.

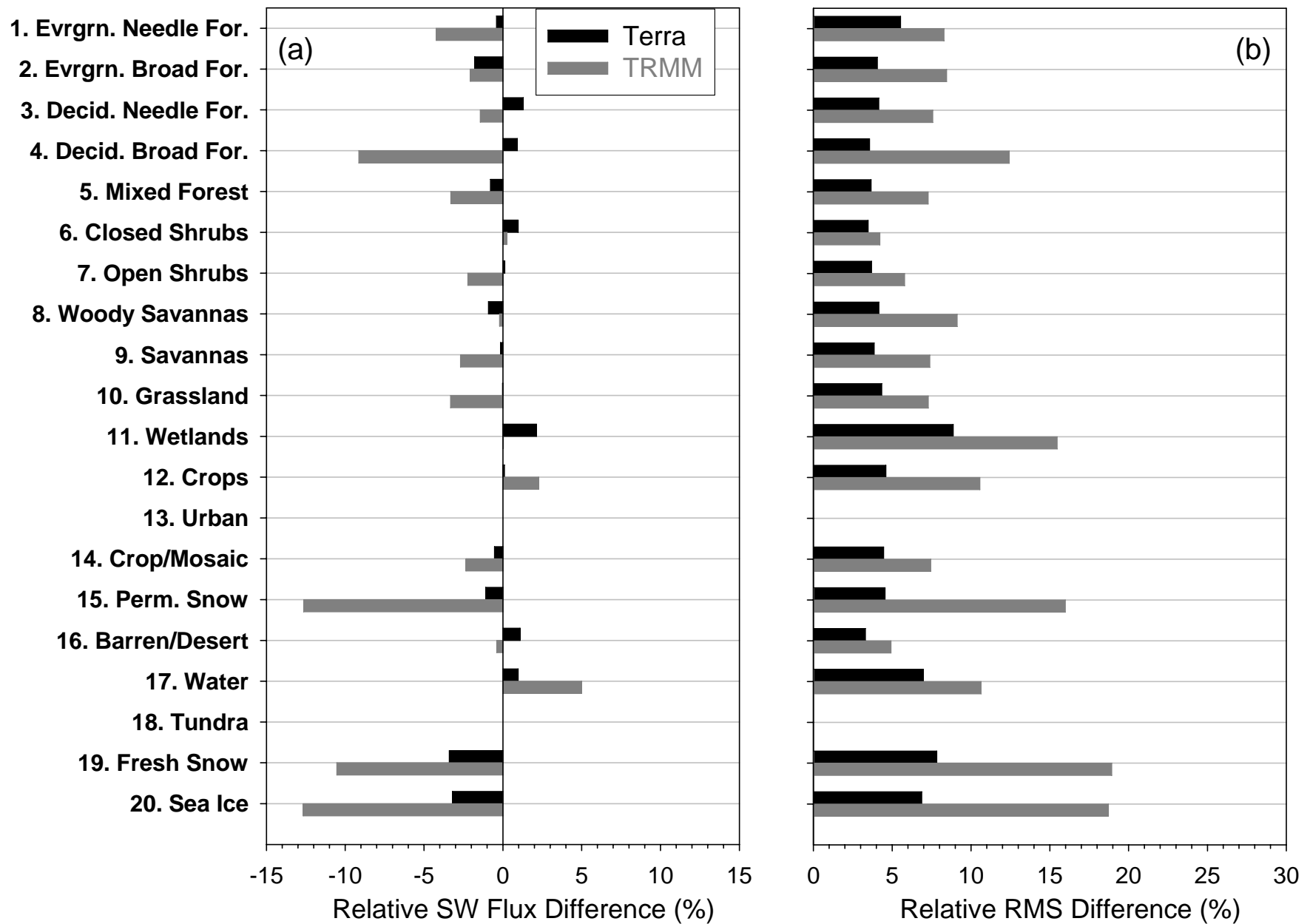


Figure 11 Clear-sky multiangle SW TOA flux consistency: (a) relative difference $[F(\theta=50^\circ-60^\circ) - F(\text{Nadir})] / F(\text{Nadir}) \times 100\%$; (b) relative RMS difference.

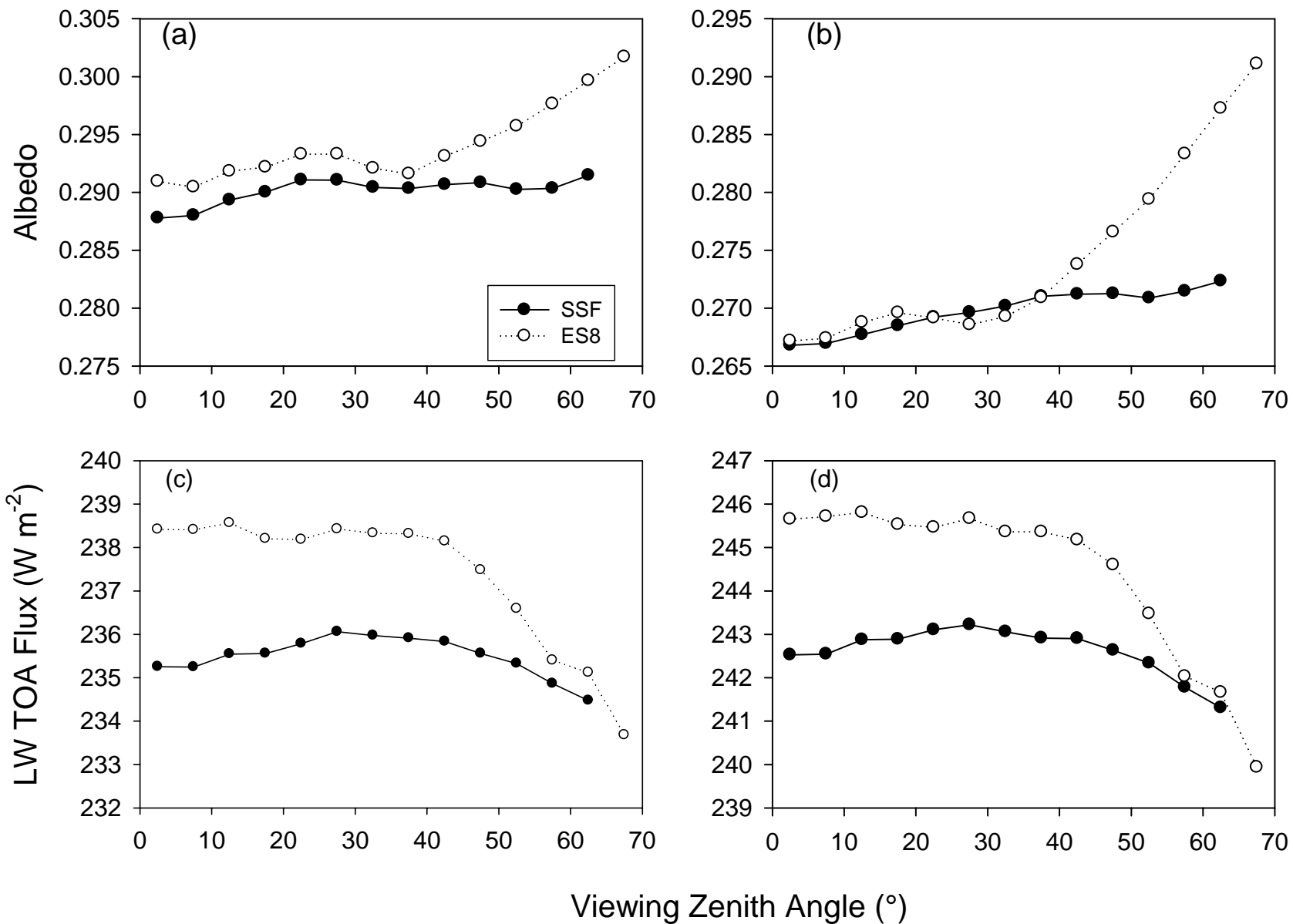


Figure 12 SSF and ES8 global albedo against viewing zenith angle for (a) January and (b) July 2003. LW TOA flux against viewing zenith angle for (c) January and (d) July 2003.

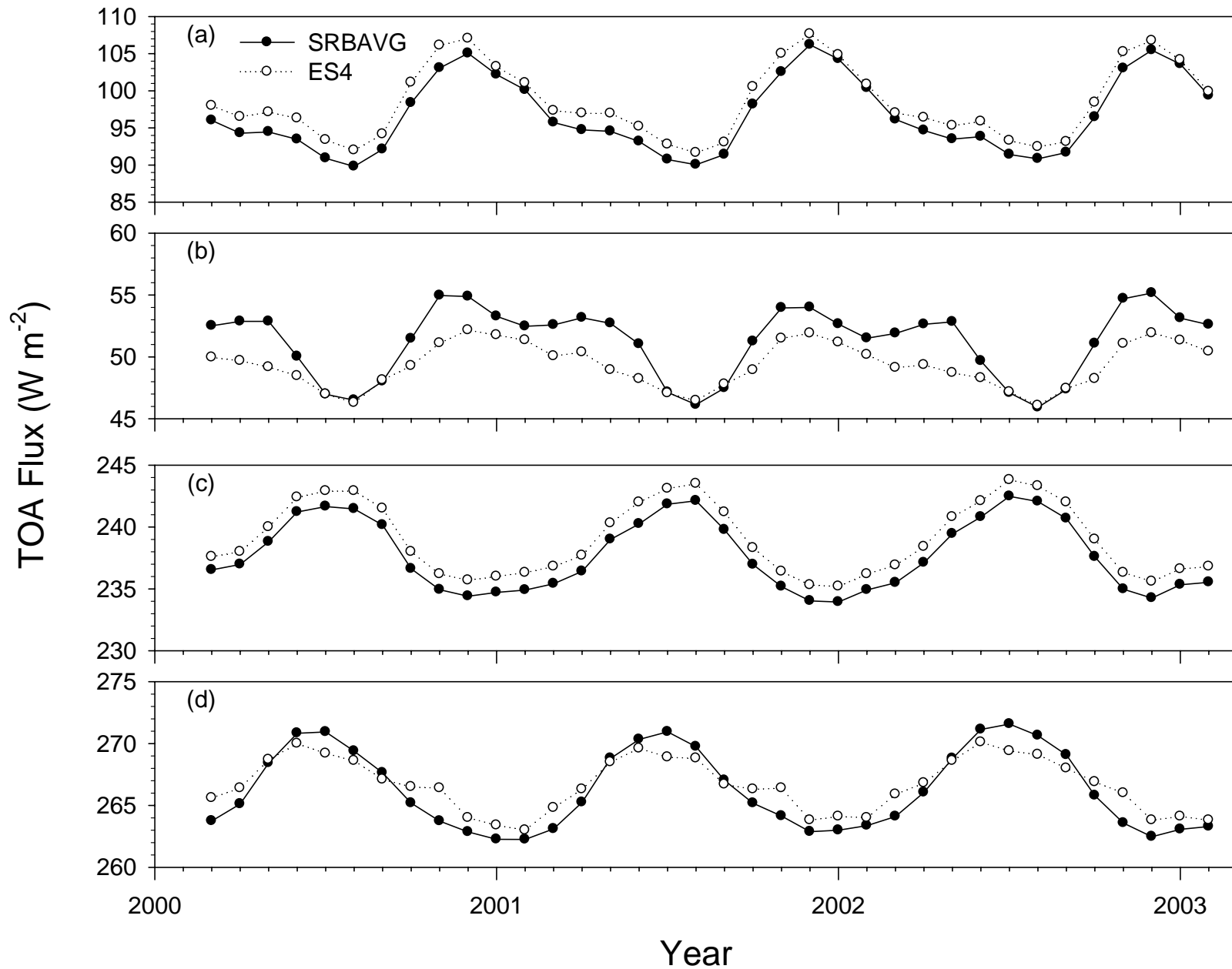


Figure 13 Global TOA flux derived from SRBAVG and ES4 products for (a) all-sky SW; (b) clear-sky SW; (c) all-sky LW; (d) clear-sky LW.

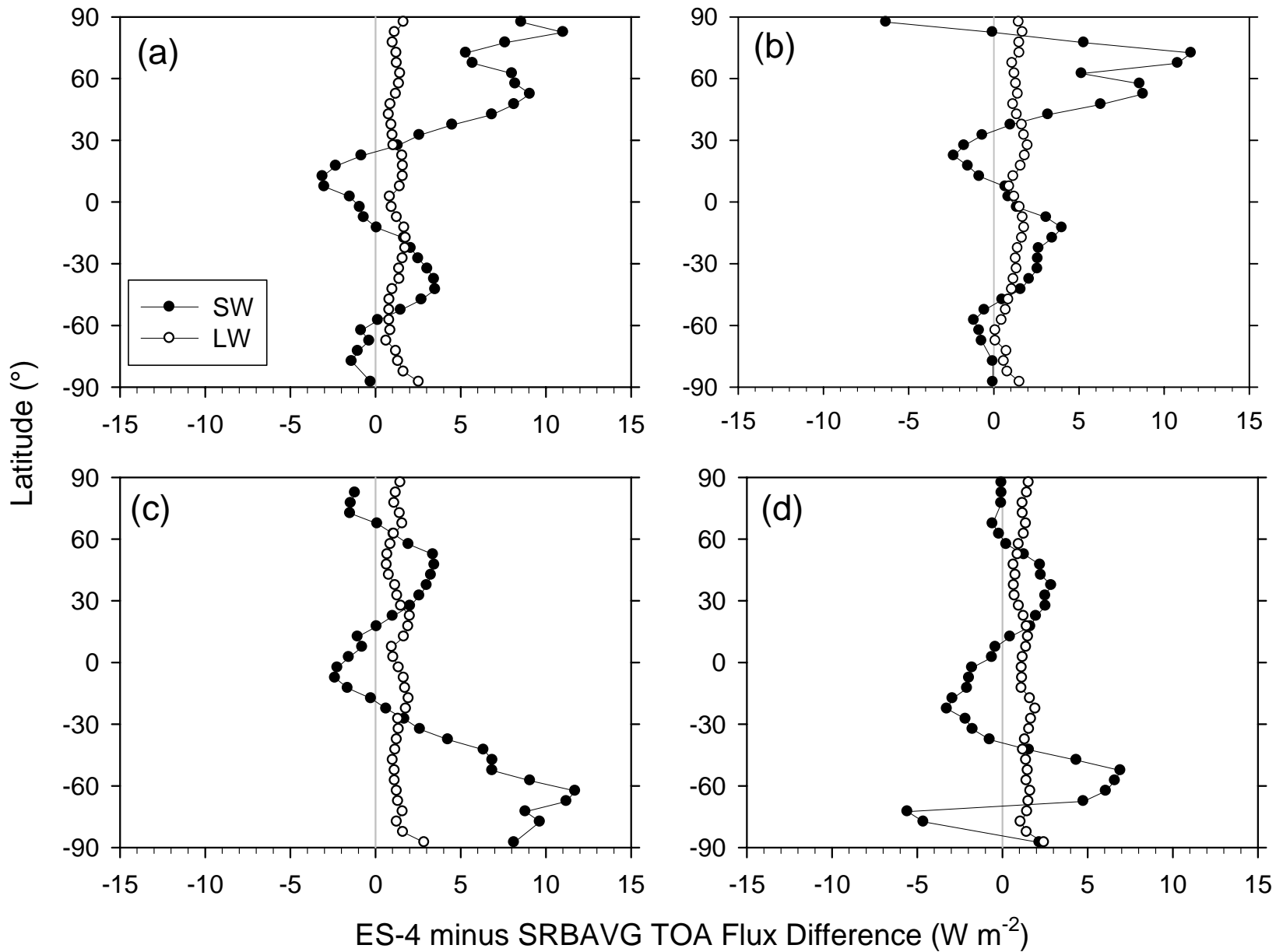


Figure 14 SW and LW TOA flux differences between the ES-4 and SRBAVG products for (a) April 2002; (b) July 2002; (c) October 2002; (d) January 2003. Zonal fluxes in both products were averaged to a common 5° latitude increment.